The contribution of volume change in preserving high-*P* metastable assemblages

Timothy Chapman[1]*, Geoffrey L. Clarke[2], Sandra Piazolo[3]

[1]*Earth Science, School of Environmental and Rural Science, University of New England, NSW, 2351, Australia.* *Corresponding author: timothy.chapman@une.edu.au

[2]*School of Geosciences, The University of Sydney, NSW, 2006, Australia.* *geoffrey.clarke@sydney.edu.au*

[3]*Institute of Geophysics and Tectonics, School of Earth and Environment, The University of Leeds, UK. s.piazolo@leeds.ac.uk*

Keywords: microstructure, fluid influx, phase equilibria, chemical–mechanical feedback, omphacite/jadeite, dynamic dilation

RUNNING TITLE

Metastability controlled by volume change

Data availability statement

EPMA and EBSD data and phase equilibria results are available within and as supplementary information to this article. Original EBSD (.h5oina) files can be requested from the author.

ABSTRACT

Incomplete retrograde reaction of sodic-calcic pyroxene occurred during the exhumation of Eocene eclogite and blueschist in NE New Caledonia. Sodic-calcic pyroxene is well-preserved in reaction relationships with paragonite and structurally late albite, in conflict with the prediction that it should transform efficiently during decompression to albite, paragonite, glaucophane and quartz. The microstructural distribution of albite accompanying crenulation cleavage development is consistent with albite growth having been restricted by space-filling requirements. In contrast, domains of high strain enable the accommodation of volume and fluid infiltration, increasing the size of the equilibration volume leading to the complete conversion of sodic-calcic clinopyroxene to albite. Despite decompression-driven dehydration, limited volume accommodation presents a plausible mechanism to metastably preserve high-*P* (up to 18 kbar) sodic–calcic clinopyroxene-bearing assemblages to lower-*P* conditions (~10 kbar) that should stabilise albite. Efficient retrogression is facilitated by dynamic recrystallisation inducing dilation.

INTRODUCTION

Mineral assemblages usually preserve just parts of a *P–T* path experienced by a given metamorphic rock (e.g. Powell et al., 2005). The ability to metastably preserve some or all a mineral assemblage at Earth's surface relates to changes in physicochemical conditions during distinct metamorphic stages (Thompson, 1955; Powell, 1983; Powell et al., 2019). The preservation of peak mineral assemblages is enabled by fluid loss during the prograde cycle, limiting any back-reaction without fluid ingress (e.g. Thompson, 1983; Guiraud et al., 2001; White & Powell, 2002; Clarke et al., 2006). Fluid ingress is commonly linked to instances of localised deformation, which can in turn contribute to reaction progression (e.g. Rubie, 1998; Carson et al., 2000; Chapman et al., 2019a, b). Infiltration sites are created by dilatational deformation, commonly in shear zones or fold hinges (Etheridge et al., 1983; Frúh-Green, 1994; Chapman et al., 2019b, Rogowitz & Huet, 2021). A preserved mineral assemblage and microstructure can reflect single or multiple stages of the metamorphic cycle, but in the absence of both fluid ingress and deformation the assemblage cannot easily back react (Schorn, 2017; Powell et al., 2019).

Sodic–calcic clinopyroxene, in the form of jadeite or omphacite, is a key index mineral of high-*P* and ultra-high-*P* metamorphism, particularly in low-variance assemblages within silicic protoliths (Carswell & Harley, 1990). Its preservation potential relates to protracted and complicated cycles of progression and retrogression (Walsh & Hacker, 2004; Palin et al., 2017; Schorn, 2022). The absence of sodic-calcic clinopyroxene from high-*P* rocks has been ascribed to kinetic limitations, fluid-poor conditions, or the metastable persistence of low-grade, often anhydrous, phases

(like albite) to high-*P* (Rubie, 1986, 1998; Koons et al., 1987; Wain et al., 2001; Proyer, 2003; Young & Kylander-Clark, 2015; Chapman et al., 2019c; Schorn, 2022). In addition, pervasive fluid influx with or without deformation at blueschist, amphibolite, or greenschist facies conditions can completely recrystalise the peak mineral assemblage (e.g. Walsh & Hacker, 2004; Schorn, 2017). A cornerstone reaction for geobarometric study involves jadeite and quartz reacting to form albite with increasing *T* and/or decreasing *P* (Holland, 1980). It is regularly used as a barometer for calibrating experimental studies due to its efficacy (e.g. Johannes, 1971). The preservation of sodic–calcic clinopyroxene in high-*P* silicic metasedimentary schists draws attention to the processes that enabled its persistence through exhumation to Earth's surface.

In high-*P* blueschist and eclogites in NE New Caledonia, sodic–calcic clinopyroxene is preserved in metapelite schists as inclusions in, or coexisting in apparent or arrested equilibrium with, retrograde albite and paragonite (Black, 1974; Clarke et al., 1997; Fitzherbert et al., 2003, 2005; Chapman & Clarke, 2021). Sodic–calcic clinopyroxene in eclogite facies assemblages is predicted to transform to albite, paragonite and/or glaucophane with quartz during decompression (Holland, 1980; Holland & Ray, 1985). The paradoxical occurrence of an anhydrous reactant and hydrous products in the same microstructure draws attention to the processes that enabled the preservation of index phases during retrogression. In this paper, the arrested back-reaction is related to both limited fluid availability and the inability to accommodate mineral volume changes due to localised absences of penetrative deformation. Using petrographic microstructures and phase equilibria modelling, these data help establish the importance of conjugate variables in understanding the preservation of prograde or peak index minerals in a broader context of host rocks that have experienced more extensive retrogression.

HIGH-P ROCKS IN NORTHERN NEW CALEDONIA

Northern New Caledonia includes a tectonically disrupted but largely coherent Eocene low-*T*/high-*P* subduction complex (Clarke et al., 1997). The effects of the metamorphism are imprinted on Jurassic to Eocene rocks that formed a micro-continent rifted from the Gondwanan Pacific margin (Fig. 1a: Aitchison et al., 1995). The high-*P* rocks have been divided into the predominately metasedimentary Diahot terrane and a MORB-type Pouébo terrane (Fig. 1b: Aitchison et al., 1995; Clarke et al., 1997). The terranes are thought to have been juxtaposed early in the uplift of the high-*P* orogen as the highest-grade rocks in the Diahot terrane record peak conditions overlapping with those of the Pouébo terrane (Fitzherbert et al., 2005).

A series of northwest-trending mineral isograds have been identified in rocks of the Diahot terrane that span lawsonite-blueschist to epidote-eclogite facies conditions (Fig. 1a; Brothers, 1974; Yokoyama et al., 1986; Black et al., 1988; Fitzherbert et al., 2005; Vitale Brovarone & Agard, 2013). The highest-grade rocks occupy the highest structural levels along the northeast coast of the Peninsula (Fig. 1b). Uranium–Pb zircon ages of narrow overgrowths on inherited zircon in the high-*P* rocks of the Pouébo and Diahot terrane falls in the range of *c.* 37–44 Ma (Spandler & Rubatto, 2005; Pirard & Spandler, 2017). Blueschist to greenschist facies retrogression and tectonism during exhumation locally complicate rock relationships (Carson et al., 2000; Rawling & Lister, 2002, Fitzherbert et al., 2005; Spandler et al., 2008). Phengite Ar–Ar ages between 34 and 37 Ma are attributed to these stages of post-peak cooling and decompression inclusive of the southwest-directed emplacement of the New Caledonian ophiolitic nappes (Cluzel et al., 1994; Ghent et al., 1994; Fitzherbert et al., 2004; Baldwin et al., 2007; Vitale-Brovarone et al., 2018; Taetz et al., 2018, 2021).

Structural geology

131 The gross geometry of terranes of the Pam Peninsula is consistent with the southwest-
132 directed stacking of progressively younger, and more deeply subducted thrust nappes
133 during terrane exhumation (D_3 and D_4: Fitzherbert, 2002; Vitale Brovarone et al.,
134 2018). A north-west trending antiformal fold (F_4), comprising a core of Diahot terrane
135 metavolcanic and metasedimentary schists, is draped by a sheet of eclogite facies
136 Pouébo terrane metabasite (Fig. 1c: Clarke et al., 1997; Rawling & Lister, 2002;
137 Fitzherbert et al., 2004). A major shear zone separating the Pouébo and Diahot
138 terranes reflects southwest-directed exhumation and thrusting late in D_2. The D_2 shear
139 zone was re-activated during D_3 in a normal sense, and locally controls breaks in
140 metamorphic grade in northeastern parts of the orogen (Fig. 1c). Additional, late-stage
141 normal faulting (D_4) locally truncates many, if not all, the metamorphic isograds
142 (Clarke et al., 1997).

143 Evidence of prograde structures (S_1 and S_2) are retained and variably
144 recrystallised by retrograde features through much of the Diahot terrane. Bedding and
145 S_1 are isoclinally folded by north-trending, reclined to recumbent F_2 folds and
146 transposed into parallelism with a shallowly dipping S_2 foliation (Fig. 1c: Clarke et
147 al., 1997). The S_2 foliation records most of the prograde metamorphic assemblage
148 progression. F_2 folds are reoriented by macroscopic F_3 and F_4 folds to form dome and
149 basin style interference patterns (Fig. 1b). F_3 folds are mostly evident in a prominent
150 S_3 crenulation cleavage; they are tight and northeast-trending with an axial plane
151 dipping steeply to the southwest (Clarke et al., 1997; Fitzherbert, 2002). Northwest-
152 trending F_4 folds are open to angular and crenulate both S_2 and S_3 into asymmetric
153 kink bands.

154 The most substantial retrogression of the Diahot terrane forms in distinct
155 zones of intense S_3 development. D_3 strain is commonly focussed in southwest-
156 dipping extensional shear zones that can be upwards of 100 metres in width. These

157 are best developed along the southwestern parts of the Peninsula. On the northeast
158 coast of the Peninsula, F_3 folds are southwest verging due to the strong influence of
159 southwest directed shearing beneath the thick sequence of comparatively competent
160 Pouébo terrane (Fig. 1c). Large areas of the Diahot terrane on the northeast coast are
161 pervasively retrogressed to blueschist–greenschist conditions (Fig. 1a). The effects of
162 D_3 retrogression are the focus of this study.

163 **Petrology of the metamorphic profile**

164 Metamorphosed parts of the Diahot terrane are predominantly interbedded pelitic and
165 volcaniclastic rocks interleaved with basic and felsic volcanics (Black, 1977;; Clarke
166 et al., 1997). Details of the mineral assemblage development in metasedimentary
167 schists can be found in Fitzherbert et al. (2003, 2005) and Chapman & Clarke (2021).
168 This work considers examples of metapelitic schist from zones 2–4 with relevant
169 omphacite–albite microstructure. Compositionally, the metapelitic schist samples are
170 aluminous with high Na_2O and CaO content and variable K_2O content. They are
171 compositionally distinct from volcaniclastic-derived metasediment in the Diahot
172 terrane (Table S1). There is a focus on samples collected from the southwestern parts
173 of the Pam Peninsula and from northwest of the township of Ouégoa in this study.
174 Samples involve those collected during recent field seasons and also from long-
175 standing collections housed at the University of Sydney (Fig. 1b). The samples record
176 variations in D_3 strain in relation to zones of macroscopic folding and shearing (blue
177 stipple on Fig. 1b)

178 Metamorphic zones defined by mineral assemblages in the Diahot terrane
179 metabasite best constrain the metamorphic field gradient (after Clarke et al., 1997;
180 Fitzherbert et al., 2003). Zone 1 mineral assemblage are characterised by the co-
181 occurrence of lawsonite, glaucophane, and omphacite (P = 8–10 kbar, T = 350–
182 400°C; Fig. 1). Zone 2 contains the lawsonite–epidote transition and can be separated

183 into zone 2a with matrix lawsonite and zone 2b delineated by the lowest *T* appearance
184 of almandine-rich garnet (*P* = 14–16 kbar, *T* = 400–550°C). Zone 3 is defined by the
185 appearance of barroisitic hornblende. The highest-grade rocks occur in zone 4,
186 marked by eclogite (omphacite-rich) assemblages (*P* = 16–18 kbar, *T* = 550–600°C).
187 ***Zone 2 metapelitic schist***
188 Most metapelitic schists in Zone 2 (9338, 96321, 23NC05A; Fig. 1b) have well-
189 developed S_2 and S_3 assemblages of glaucophane, albite, clinozoisite, garnet,
190 phengite, paragonite, titanite, chlorite, and quartz with or without omphacite, jadeite
191 and/or rutile (Figs 2a–b & 3a–c; Clarke et al., 1997). The inferred peak S_2 assemblage
192 comprises spessartine, lawsonite, omphacite–jadeite, clinozoisite, ferroglaucophane,
193 phengite, paragonite, titanite, and quartz. Co-occurrences of lawsonite and
194 clinozoisite in the matrix of the schists are found only in zone 2a near the zone 1–2a
195 boundary (2013: Figs 1b & 3c). In zone 2b, garnet (2–3 mm in diameter) has grain
196 cores with inclusion trails of S_1 titanite and graphite enclosed by quartz–clinozoisite-
197 bearing rims.
198 Coarse-grained poikiloblasts of albite have cores with inclusions of S_2
199 ferroglaucophane, paragonite, phengite, and garnet, with or without jadeite and
200 omphacite (Figs 2a–b). Needles of omphacite and glaucophane can form randomly
201 orientated inclusions in albite (Figs 2a & b). The boundaries of albite grains are
202 commonly pinned between foliation planes or bedding partings (Fig. 2b). Layers rich
203 in albite lack substantial omphacite and vice versa (Fig. 2b).
204 Albite occurs in higher modes in regions of high D_3 strain and presents in two
205 morphologies: (1) as irregular grains aligned within S_3 that host inclusions trails of
206 phengite, paragonite, glaucophane and chlorite (Fig. 2c); and (2) as facetted grains
207 with simple twins. The grain boundaries of adjacent albite crystals are oriented at high

208 angles to bedding and S_2. S_3 and S_4 chlorite partially pseudomorphs glaucophane (Fig.
209 3b).
210 ***Zone 3 metapelitic schist***
211 The metapelitic schists of zone 3 commonly contain S_2 omphacite and garnet
212 porphyroblasts (up to 5 mm in diameter: Fig. 2d). Simply twinned albite occurs
213 throughout zone 3 schists with modes between 10 and 30%. Where albite is common,
214 omphacite is less common and vice-versa. The distribution of albite and omphacite
215 again reflects the intensity of D_3 strain. Samples described here occur within (WC21),
216 or proximal to (9403, 9927), a 100 m wide D_3 shear zone located on the southwest of
217 the Pam Peninsula (Fig. 1b). The inferred peak S_2 mineral assemblages in zone 3
218 involve combinations of garnet, omphacite, paragonite, phengite, clinozoisite,
219 glaucophane, quartz, and rutile.
220 Metapelitic samples distal to rocks with intense D_3 strain (e.g. 9927) have
221 coarse-grained S_2 garnet, omphacite and glaucophane porphyroblasts that are
222 intergrown with phengite, paragonite, quartz, graphite and rutile (Fig. 2c). Garnet
223 grain cores host S_1 inclusion trails of graphite, titanite and quartz. Rectangular
224 pseudomorphs of clinozoisite and paragonite after S_1 lawsonite occur in some garnet
225 grain cores. Garnet grain rims have S_2 inclusion trails of quartz, clinozoisite and
226 minor omphacite. Rutile in the rock matrix is rimmed by titanite. Rectangular
227 omphacite (200–400 μm in length) occurs in clusters defining S_2, and may be
228 commonly intergrown with, or partially enclose randomly oriented glaucophane (Fig.
229 2e). Omphacite can have an interlobate or epitaxial growth texture with paragonite
230 and phengite.
231 Samples within or along the edge of a large D_3 shear zone (WC21 and 9403,
232 respectively; Fig. 1b) show varying extents of omphacite and paragonite being
233 overgrown by albite poikiloblasts (Fig. 2e). Minerals defining S_2 are enveloped or

234 partially pseudomorphed by combinations of S_3 phengite, paragonite, glaucophane,
235 clinozoisite, rutile, titanite, graphite, and quartz. This replacement texture initially
236 takes the form of a crenulation cleavage that becomes an intense shear fabric where
237 more developed. Albite occurs as large, elongate and asymmetric poikiloblasts either
238 aligned with S_3 or as simply twinned overgrowths on crenulated or disjunctive S_2–S_3
239 folia, consistent with them forming syn- to post-D_3 (Figs 2d & 4). The cores of albite
240 poikiloblasts common contain S_2 inclusion trails of garnet, omphacite, glaucophane,
241 paragonite, rutile and quartz (Fig. 3e). The rims of albite tend to be comparatively
242 inclusion-poor, but host clinozoisite, glaucophane, paragonite, chlorite and phengite
243 inclusion trails that are continuous with the external S_3 foliation (Fig. 2e). Typically,
244 omphacite in the matrix is preserved in strain-shadows of garnet porphyroblasts or
245 away from hinge zones of S_3 crenulations (Fig. 2d). It occurs as delicate elongate
246 grains intergrown with paragonite, phengite and rutile. Chlorite intergrown with
247 phengite in the matrix is partially to completely pseudomorphed by stilpnomelane.
248 ***Zone 4 metapelitic schist***
249 The metapelitic schist from zone 4 occurs in the hinge of an F_3 fold (23NC20B; Fig.
250 1b) and contains comparatively little albite (5–10%). The inferred peak S_2 mineral
251 assemblages comprise garnet, omphacite, paragonite, phengite, rutile, quartz with less
252 winchite and clinozoisite than in zone 3 samples. The S_2 foliation is defined by
253 segregated cm-scale phengite, paragonite, omphacite and winchite in layers separated
254 from quartz and garnet (Fig. 3f). Some layers are locally rich in graphite. A prominent
255 S_3 crenulation cleavage reorients the S_2 foliation (Fig. 3f). Coarse-grained (cm-scale)
256 garnet poikiloblasts retain snowball S_2 inclusions trails of quartz, chlorite and
257 graphite. Rims have inclusions trails of quartz and omphacite continuous with the
258 matrix S_3 folia. Mica-rich (M) domains (Vernon, 1989) comprise phengite laths
259 intergrown with paragonite, commonly with interpenetrated sheets. Omphacite is

prismatic or acicular and occurs aligned with both S_2 and S_3 (Figs 3g & 4d). When in S_3 folia, omphacite is surrounded by paragonite, idioblastic winchite or albite (Fig. 4f). Clinozoisite forms tabular crystals either as coronae to titanite or omphacite and in grains with allanite cores defining S_2 (Fig. 4f). Late, simply twinned albite poikiloblasts (cm-scale in diameter) form in the hinges (83%) of the S_3 crenulation cleavage (quartz-rich Q-domains) are rarely in mica-domains (M-domains) (17%: Figs 3f–g & 4e). S_2 inclusion trails to albite comprise titanite, omphacite, phengite and clinozoisite (Fig. 4e). Omphacite is more abundant as inclusions in grain rims. The edges of albite grains are irregular and commonly inter-fingering with matrix paragonite and phengite, consistent with epitaxial growth (Fig. 4e). Chlorite forms as late overgrowths on garnet or in the rock matrix, partially pseudomorphous to glaucophane.

METHODS

Electron microprobe

The major element content of the rock-forming minerals was determined using a JEOL JXA-8530F plus field emission electron microprobe housed at the Central Science Laboratory at the University of Tasmania, a hub of Microscopy Australia. Operating conditions involved a 15 kV accelerating voltage and 20–30 nA beam current. Analyses were collected using five wavelength dispersive spectrometers (WDS) using TAP, LPET, PET, and LLIF crystals. Maps of X-ray intensity for sample WC21 (Fig. 4) were collected during earlier studies as part of Fitzherbert et al. (2005) on a Cameca SX-50 Camebax microprobe housed at the University of New South Wales. The maps were collected at 10 μm step sizes with a 15 kV accelerating voltage, a 1–3 μm beam size and count times of 300 milliseconds at each point. Matrix correction for data points forming the maps follows the method outlined in Clarke et al. (2001).

Quantitative orientation analysis: Electron backscatter diffraction

Electron back-scatter diffraction analysis (EBSD: Figs 5–7) was performed using a FEI Quanta 650 FEG SEM with the Oxford Instrument Symmetry detector at the Bragg Centre for Materials Research at the University of Leeds, UK and a Hitachi SU-70 field emission SEM at the Central Science Laboratory at the University of Tasmania. Etched polished thin sections (~30 μm) were analysed at an accelerating voltage of 20 kV, with a beam current of 8 nA and a working distance of ~9–25 mm. Electron backscatter diffraction patterns were automatically acquired and indexed using Oxford Instruments AzTEC software (https://www.oxford-instruments.com/). The EBSD patterns were collected in regular grids where the sampling step size was 5 μm. Postprocessing was undertaken in the Oxford Instruments AzTEC crystal software following procedures that are designed to remove false data and to enhance data continuity over the microstructures (Piazolo et al. 2006). In the analysis, grains are defined as areas enclosed by boundaries of greater than 10° of misorientation; boundaries with misorientation less than 10° but greater than 1° are referred to as low-angle boundaries (e.g. Piazolo et al. 2006; Chapman et al., 2019b).

Phase Equilibria Modelling

Phase equilibria modelling (Figs 8–10) was performed using THERMOCALC (Powell & Holland, 1988) in the NCKFMASHTO chemical system (Na_2O–CaO–K_2O–FeO–MgO–Al_2O_3–SiO_2–H_2O–TiO_2–O) utilising version 3.50 (Powell & Holland, 1988) and the internally consistent thermodynamic dataset 6.2 (updated 6th February 2012: Holland & Powell, 2011). The model compositions encompass a zone 3 metapelite (WC21) determined from X-ray element maps (Fig. 4, after Fitzherbert et al., 2005).

Redox conditions were fixed at $Fe^{3+}/[Fe^{3+}+Fe^{2+}] = 0.1$ (Chapman & Clarke, 2021). Fluid (H_2O–H: Evans & Powell, 2015) was fixed to saturate the lowest-*T* and

highest-*P* equilibria (H_2O = 13.42 mole %). The fluid remains at high aH_2O (>0.99) throughout the model conditions, thus H_2O contours are shown and discussed in units of mole percent relative to the normalised bulk H_2O content ignoring the contributions of H. Mineral activity–composition models and abbreviations include: glaucophane (gl), actinolite (act), hornblende (hb), jadeite/omphacite/diopside (jd/o/dio: Green et al., 2016), feldspars (abc, pl, & kfs: Holland et al., 2021), garnet (g), paragonite (pa), biotite (bi), muscovite (mu), chlorite (chl: White et al., 2014a), epidote (ep: Holland & Powell, 2011), chloritoid (ctd), talc (ta: Rebay et al., 2023). Stilpnomelane (stp) *a–x* model utilises ideal mixing of the Mg-stilpnomelane and Fe-stilpnomelane endmembers following Miyano & Klein (1989) after Holland & Powell (2011). Phases treated as pure include lawsonite (law), rutile (ru), titanite (sph), quartz (q), and kyanite (ky).

There is limited variability in bulk composition across metapelite of the various zones in the Diahot Terrane, except for ratios of CaO, Na_2O and K_2O (Table S1). Adjustments in these ratios impact the stability of sodic-calcic pyroxene at low-pressure conditions, but omphacite and/or jadeite remain stable at high-pressure conditions (>15 kbar). These variables alone cannot account for the coexistence of albite and sodic-calcic pyroxene in the microstructures. The limited compositional variability between low- and high-strain samples supports the application of one bulk composition for the calculated phase equilibria for the different samples.

Limitations in activity–composition models for Mn in clino-amphibole, epidote, clinopyroxene, sphene and mica restrict the general applicability of modelling in the MnNCKFMASHTO system at high-pressure (e.g. White et al., 2014b). The effect of incorporating MnO into the model system on garnet growth was evaluated by Chapman & Clarke (2021) using the expanded MnNCKFMASHTO system, and activity–composition models of White et al. (2014b). Garnet growth

338 extends to lower-T (~50°C) in MnNCKFMASHTO and has minimal impact on sodic-
339 calcic clinopyroxene, clino-amphibole and mica modes (<1–2%) and only partially
340 extends chlorite stability. These have minimal influence on inferred retrograde
341 reactions or the volume changes.
342 Validation of the predicted phase equilibria relative to the observed mineral
343 assemblages was considered based on mineral mode (cf. Fig. 11). The calculated fluid
344 retained within hydrous phases was compared from preserved mineral assemblages
345 assuming stoichiometric H_2O and hydroxyl from zones 1–4 and sample from within a
346 D_3 shear zone (9338) against those predicted at the notional peak metamorphic
347 conditions and associated with retrogression completed at the blueschist–greenschist
348 boundary for the D_3 event. The same comparison was completed for density (ρ), and
349 volume (ΔV) for natural samples and compared relative to predicted peak conditions
350 from the phase equilibria modelling. Comparative reaction progress (ξ) was
351 considered as the mode adjustment between albite–paragonite–omphacite as these
352 phases change by more than 10% over the blueschist–greenschist transition.
353 A P–M_{H2O} pseudosection was calculated to assess the influence of water
354 content on the stability and preservation of high-pressure phases during exhumation at
355 fixed T = 460°C (Fig. 9a). This temperature was selected as it best matches the
356 conditions of retrogression for zone 2 and 3 metapelitic schists that contain the
357 greatest abundance of albite–omphacite-bearing microstructures (Clarke et al., 1997;
358 Fitzherbert et al., 2005). Portions of the initial decompression path are not-strictly
359 applicable to the P–M_{H2O} pseudosection due to temperature differences between the
360 notional peak conditions and that of D_3 retrogression (Fig. 8a). However, variation in
361 in the predicted H_2O retained by hydrous minerals is small between the T of 460°C
362 and 525°C for zone 2 and 3 schists and thus the analysis provides both indicative and
363 partially quantitative results (cf. Figs 9 & 11). Unrecognised fluid-loss events may

have also occurred along any *PT* path and may have introduced generalities for many low-variance fields.

Conjugate *V*–*T* and *V*–M_{H2O} pseudosections were also determined to account for the role of *V* change in the preservation of mineral phases (Figs 9b & 10). Absolute and relative volume changes for both solids and free intergranular fluid are quantified based on the normalised molecular mass of the modelled bulk composition at the specific *PT* conditions (Powell et al., 2005).

MINERAL COMPOSITION

The aegirine (*Aeg*) content of clinopyroxene in metapelitic rocks decreases with grade through much of the zone 2 with limited variation in quadrilateral component (*Q*: Morimoto, 1989). Grain cores have $Jd_{30–48}Aeg_{0–48}Q_{22–48}$ and rims $Jd_{37}Aeg_{29}Q_{34}$. Locally, jadeite ($Jd_{86–98}Aeg_{2–10}Q_{3–12}$) and omphacite ($Jd_{44–48}Aeg_{9–10}Q_{42–44}$) co-exist. In zones 3 and 4 omphacite in the metapelitic schists has limited within and between sample variation involving $Jd_{38–60}Aeg_{0–10}Q_{40–52}$. There is minor core to rim increase from $Jd_{38–46}$ to $Jd_{47–60}$.

Albite is nearly always close to the pure endmember ($Ab_{96–100}An_{0–4}$). There is limited variation across all the zones, lithologies and grains attributed to prograde *versus* retrograde growth.

The silica content of S_2 phengite in metapelitic schists of zones 2–4 define a linear trend from 3.3 Si (per 11 oxygens formula unit) to 3.55 Si cations. This matches a general decline in the soda content of phengite. S_3 phengite has lower silica values <3.43 pfu.

Clino-amphibole in the metapelitic schists varies from ferroglaucophane to glaucophane and winchite (after Leake et al., 1997). Ferric content and site distribution were calculated according to Robinson et al. (1982). The transition from ferroglaucophane to glaucophane occurs in the upper parts of zone 2 (Fitzherbert et

al., 2005). X_{Mg} is between 0.3 and 0.7, and silica cations between 7.8–8 based on per formula unit of 16 oxygens. In zone 3, amphibole is mostly glaucophane with X_{Mg} of 4.9–7.2 though it can be crossitic (X_{Fe3+} = 0.07–0.38). Winchite and barroisite (X_{Na} = 0.35–0.6 and silica contents of 7.2–7.8 cations) are also present in zone 3 but more common in zone 4 metapelitic schists.

Garnet in zone 2 has core to rim zoning from $Grs_{17–21}Alm_{41–45}Sps_{25–35}Prp_{1–2}$ to $Grs_{31–38}Alm_{46–60}Sps_{2–14}Prp_{1–3}$. A bell-shaped decrease in spessartine content is pronounced, and garnet is almandine rich. In zone 2 samples with high D_3 strain, core to rim zoning involves a subtle rimward increase in spessartine content consistent with resorption. In zones 3 and 4, garnet is comparatively enriched in almandine and grossular and depleted in spessartine. There is rimward zoning from cores of $Grs_{21–29}Alm_{50–57}Sps_{6–28}Prp_{1–8}$ to $Grs_{23–32}Alm_{57–67}Sps_{1}Prp_{7–10}$. The progression is generally concentric. Garnet in zone 4 schists only locally has spessartine-rich cores and mostly flat core–rim profiles.

Clinozoisite in the metapelitic schists has a marked decrease in ferric content between zones 2 and 3. The Czo content ([Al–2]/[Al–2+Fe^{3+}]) ranges from 0.27 in zone 2 to 0.9 in Zone 3. Much of the clinozoisite in zones 3 and 4 cuts S_2 and has Czo = 0.45–0.6. There is no significant compositional variation between S_2 and S_3 clinozoisite. Rare instances of S_4 clinozoisite associated with albite has Czo values ranging from 0.4 to 0.57.

MICROSTRUCTURE

Focussed EBSD maps were collected over albite poikiloblasts from samples 2013, 23NC05A, 9403, and 23NC20B (Figs 5–7). Difficulties in the polish quality of mica grains resulted in poor indexing of phengite and paragonite, unless they were suitably orientated.

Zone 2 (Sample 2013 & 23NC05A)

The metapelitic schist from Zone 2a (2013) has an incipient S_3 crenulation cleavage defined by phengite, paragonite, glaucophane, and quartz that produces a prominent CPO. Lawsonite, clinozoisite, omphacite, and jadeite only retain weak CPO. Albite poikiloblasts form mostly in Q-domains (Fig. 5a), commonly in association with large (400 μm), deformed but idioblastic lawsonite (up to 10° of distortion). The large albite poikiloblasts (600 μm) have simple twins that have overgrown the bent S_2 foliation now preserved as inclusions trails of quartz, glaucophane, lawsonite, omphacite or jadeite (Fig. 5). Albite mostly lacks crystal distortion, except for localised rims that can have misorientation of 3–4° (Fig. 5c). Small inclusions of jadeite (<100 μm) in the grain cores retain coincident crystallographic axes with albite consistent with epitaxial growth (Fig. 5b).

Sample 23NC05A formed in a high-strain D_3 shear zone in zone 2b and comprises high albite mode (~20%). The albite poikiloblasts (up to 600 μm) have limited crystal distortion (up to 10°), and a strong SPO defining asymmetric growth (Fig. S1). Typically, they are intergrown with clinozoisite, phengite, and glaucophane but lack a CPO consistent with late-D_3 growth (Fig. S1). Glaucophane forms as large porphyroblasts (200 μm) with crystal distortion (up to 10°) and finer elongate and relatively undeformed grains defined by a prominent CPO ((010) and (001) in the foliation plane) consistent with the operation of dissolution-precipitation creep (Figs S1 & S2). Quartz forms elongate ribbons that have accommodated crystal bending (up to 15°) by slip on the basal plane. Smaller, recrystallised quartz grains retain a strong CPO (Figs S1 & S2).

Zone 3 (Sample 9403)

The sample 9403 contains S_2 folia transposed and rotated into a semi-penetrative S_3 fabric. Albite poikiloblasts retain inclusion textures involving combinations of omphacite (~100 μm) that are closely intergrown with rounded quartz, and elongate

442 glaucophane, and paragonite that has crystallographic alignment associated with
443 penetrative fabrics of either S_2 or S_3 in the rock matrix (Fig. 6a). Albite poikiloblasts
444 have 5–6° of internal crystal distortion. However, most of this distortion is localised
445 along the grain edges and associated with deformation (Carlsbad) twins, or low-angle
446 boundaries consistent with its syn- to late-S_3 growth (Fig. 6a). Omphacite, quartz and
447 glaucophane inclusions in albite have crystal distortion (0.5–3°) over length scales of
448 30–100 μm. Matrix quartz and glaucophane have greater distortion of upwards of 10°
449 mostly on low-angle grain boundaries. S_3 glaucophane and paragonite form as
450 elongate grains intergrown along the edges of albite poikiloblasts (Fig. 6a). Internal
451 domains of the albite grains have limited distortion (<1°) and can contain growth-
452 related albite law twins (Fig. 6a & c). The albite {100} crystal axes are oriented
453 within the foliation and the{001} axes oriented normal to the foliation, inheriting
454 aspects of omphacite axes via epitaxy or topotaxy along the [010] axis
455 ($[010]_{ab}||[010]_o$; Fig. 6b).
456 *Zone 4 (Sample 23NC20B)*
457 Sample 23NC20B has a prominent S_3 crenulation cleavage separating M-domains
458 rich in phengite, paragonite, clinozoisite, with less clinozoisite, titanite, glaucophane,
459 albite, and omphacite, from Q-domains of quartz, honeycomb garnet, omphacite, and
460 albite (Figs 7a–g). Omphacite, mica, quartz, and amphibole are bent and rotated into
461 the zonal crenulation cleavage (Figs 7a–c & S3). Rotation associated with the
462 development of F_3 hinges can lineate acicular omphacite along (100) axes. Omphacite
463 is deformed plastically, involving crystal distortion of up to 10° mostly along low-
464 angle boundaries with rotation around the (001) axis (Figs 7a, h & S3). Quartz has
465 greater disorientation (up to 17°), and the development of higher proportions of
466 Dauphine twins in grains forming on the margin of M-domains relative to Q-domains
467 (up to 7°: Fig. 7b). Together with its low-angle boundary development it suggests the

activation of the rhomb <a> slip system during sub-grain rotation recrystallisation (Fig. 7h). Aligned and rotated quartz inclusion trails in albite and garnet typically have greater crystal distortion (17°) relative to the matrix grains (Fig. 7a–c). Clinozoisite and titanite preserve a CPO within S_3 though lack internal misorientation similar to mica and amphibole suggesting they were all deformed by dissolution–precipitation creep (Fig. S3).

Large albite poikiloblasts (750–1500 μm) form in hinge zones of Q-domains (nearly 83% of albite volume), with only smaller grains (<750 μm) forming in the M-domains (~17% by volume: Fig. 7d–f). Irregular albite morphologies in the hinges mimic the folded overgrown precursor omphacite and paragonite, and contain only aligned intergranular quartz or omphacite inclusions. Coincident albite (100) faces with paragonite (001) reflect pseudomorphous growth to produce the irregular crystal form appearing to mimic $(001)_{pa}||(100)_{ab}$ epitaxial growth, though indexing of paragonite remains challenging. Despite the contorted albite habit there is minimal plastic distortion (up to 4°: Fig. 7a & c). Any distortion is restricted to low-angle boundaries near the grain rims and likely reflects recovery of lattice bending to accommodate space for its growth late in D_3 (Fig. 7c). Albite in M-domains has substantial more lattice distortion (15°) associated with higher-strain and the relative strength of adjacent phases (e.g. garnet: Fig. 7a).

PHASE EQUILIBRIA MODELLING

Mineral equilibria predicted for Diahot metasediment WC21 involves mostly quadrivariant fields over moderate to large *T* ranges (Fig. 8a). Narrow, lower-variance fields are restricted to the boundaries of the key metamorphic facies. The transition from greenschist to blueschist (*T* = 350–500°C and *P* = 9–11 kbar) involves a progression from quadrivariant assemblages with albite and stilpnomelane to assemblages with glaucophane and omphacite, over a *P* interval of 2–3 kbar (Fig. 8a).

In the lawsonite stability field, the greenschist–blueschist boundary (T = 300–375°C and P = 9–11 kbar) is displaced by the clinozoisite–lawsonite transition and the solvus of jadeite and omphacite over a T range of 20–30°C (Fig. 8a). Narrow trivariant fields involving the clinopyroxene solvus and the lawsonite–epidote transition delineate the boundary between lawsonite and epidote blueschists for increasing pressure conditions. The clinopyroxene solvus converges at P =19 kbar and T = 560°C in a broad quadrivariant field involving garnet but lacking epidote (eclogite facies; Fig. 8a). The transition from the greenschist or epidote blueschist (T = 375–500°C and P = 9–11 kbar) to amphibolite facies (T = 450–500°C and P = 5–12 kbar) involves a series of closely-spaced trivariant and divariant fields including the hornblende–glaucophane solvus, the stabilisation of chlorite and biotite and the peristerite gap (immiscibility between Na–Ca feldspars: T = 400–500°C and P = 5–11 kbar) (Fig. 8a & c).

P–T path

The equilibria predicted for the metapelitic compositions are consistent with the distribution of the natural assemblages and *P–T* estimates made for samples across the Pam Peninsula (Black et al., 1988; Carson et al., 1999, 2000; Marmo et al., 2001; Fitzherbert et al., 2003, 2005; Clarke et al., 2006; Vitale Brovarone & Agard, 2013; Chapman & Clarke, 2021). The identification of a series of metamorphic zones is related primarily to S_2 assemblages (Clarke et al., 1997; Fitzherbert et al., 2003; Chapman & Clarke, 2021). 'Peak' conditions in each zone best correspond to the following quadrivariant fields: zone 1 gl–law–ab–pa–sph–mu–q; zone 2a pa–gl–o–law–sph–mu–q; zone 2b pa–gl–o–ep–ru–mu–q; zone 3 g–pa–l–o–ru–mu–q; zone 4 g–pa–gl–jd–ru–mu–q (Fig. 8a). The prograde *PT* path of the Diahot metapelites is likely at slightly colder conditions than the preserved notional peak conditions of each zone in the field array. However, it remains difficult to resolve the difference between *T*

before any thermal relaxation on the prograde heating path, it appears to have been small (Vitale Brovarone et al., 2018; Chapman & Clarke, 2021). The details of the prograde history are considered in detail by Chapman & Clarke (2021) and not further explored here.

The main sites of fluid loss along the inferred prograde path correspond closely to low-variance boundaries of the metamorphic facies, specifically those that are *T*-dependent (Fig. 8b). Along the inferred prograde path, the metapelitic schists are predicted to release between 3 and 9.5% moles of H_2O-rich fluid from zones 1 to 4 (Figs 8a & 11a). Prograde *PT* trajectories at lower temperature than the field array would induce similar fluid-loss histories. At the notional peak conditions, only H_2O structurally bound in minerals is retained in the system, with limited amounts plausibly also in nominally anhydrous phases. The predicted modes of hydrous minerals at peak conditions corresponds to the retention of between 9.7–4% moles of equivalent H_2O (Fig. 11a). The predicted modes of hydrous phases at peak conditions of the metamorphic zones overlap with observed modes preserved in metapelitic schists (Fig. 11). These H_2O values are the key thresholds to overcome for closed-system back-reaction without additional H_2O ingress.

Retrograde PT path

The *PT* path of rocks returned from each of these zones can be defined based on features preserved in inclusion–porphyroblast relations and assemblages in late folia and other structures. A divergence in retrograde history is apparent between the lawsonite-bearing versus epidote-bearing portions of the Diahot terrane. The preservation of lawsonite in schists of zone 1 and 2a is consistent with a hairpin-style path involving substantial cooling at pressure conditions entirely within lawsonite stability (blue paths in Fig. 8a: Clarke et al., 2006; Vitale Brovarone et al., 2018). Limited late metamorphic recrystallisation is mostly associated with faults and shear

546 zones, though the partial replacement of glaucophane by stilpnomelane and chlorite
547 can also be pervasive (Clarke et al., 1997; Fitzherbert et al., 2005). It is challenging to
548 distinguish prograde and retrograde albite in the metapelitic schists. Exhumation
549 trajectories for the higher grade metapelitic schists (above zone 2b) involve partial
550 overprinting in the epidote stability field (Fitzherbert et al., 2005). It is the high-grade
551 schists that are the primary focus of the mineral preservation history.
552 The initial stages of decompression in the Eocene orogen are inferred to have
553 occurred during the later stages of S_2 development (Fig. 8a: Bell & Brothers, 1985;
554 Clarke et al., 1997; Fitzherbert et al., 2005). Features that are consistent with this
555 interpretation include the overlap of the peak S_2 conditions in the Diahot and Pouébo
556 terranes, and the seeming continuity in the orientation of S_2 across the terrane
557 boundary (Clarke et al., 1997). In the metapelitic schists, S_2 and sometimes S_3
558 inclusion trails commonly pass straight through large, commonly twinned, albite
559 grains without deflection or the development of strain shadows. In addition,
560 omphacite seems stable in S_3 crenulations. These relationships are consistent with
561 albite growth at the expense of omphacite and paragonite syn- or post-D_3.
562 Additionally, clinozoisite is abundant in zone 3 and 4 schists consistent with its
563 growth at the partial expense of garnet and omphacite mode during early cooling. The
564 initial stages of albite growth were followed by the development of an intense D_3
565 crenulation of earlier flat-lying fabrics during exhumation through epidote blueschist
566 facies conditions (red portions of *path* in Fig. 8a: P = 11–14 kbar and T = 450–500°C:
567 Fitzherbert et al., 2005). This stage accompanied most albite growth involving a
568 noticeable increase in predicted mode during decompression over the multivariant
569 blueschist–greenschist boundary (1–10% mode change). Later greenschist facies
570 retrogression (P = 6–9 kbar and T = 400–450°C) involved another stage of kink
571 banding related to D_4 structures. Steeply dipping S_4 folia are defined by

572 stilpnomelane–chlorite–albite–phengite–epidote-bearing assemblages (Clarke et al.,
573 1997; Carson et al., 2000; Fitzherbert et al., 2005).
574 The near ubiquitous distribution of pure albite necessitates some cooling
575 (~50–150°C) from peak conditions during the unroofing (~6–10 kbar) event, to
576 remain at *T* below the peristerite gap (*T* = 425–500°C and *P* = 9–11 kbar: Fig. 8c).
577 The general structural coherence of fabrics across zones 1 to 4 as well as the short
578 timeframes of the closure of many of the isotopic systems suggest that cooling
579 occurred early in the exhumation history (Baldwin et al., 2007; Vitale Brovarone et
580 al., 2018). This prediction is supported by minimal epidote growth due to the small
581 difference in retained hydrous mineral content from the notional peak metamorphic
582 conditions across the 50–150°C cooling interval (Fig. 11). Much of the S_3 omphacite–
583 albite microstructures therefore reflects late-stage near isothermal (~450–480°C)
584 decompression (2–6 kbar) during F_3 folding associated extensional shearing.
585 *Omphacite–albite transition*
586 The omphacite– albite transition occurs at *P* of 9–12 kbar in a narrow trivariant field
587 (Figs 8a & c). The field expands subtly in lawsonite-bearing equilibria and the two-
588 pyroxene solvus. These conditions match but are at lower-*P* than the predicted
589 location of the degenerate pure jadeite + quartz = albite reaction that occurs at
590 pressure of between 10 and 15 kbar at temperatures of 350 to 550°C (Fig. 8a: Newton
591 & Smith, 1967; Holland, 1980; Koon & Thompson, 1985; Liu & Bohlen, 1995). A
592 pressure-dependence of the reaction is known to be influenced by *a*–*X* relations and
593 the structural states of sodic clinopyroxene and plagioclase (Holland, 1980; Wood et
594 al., 1980). The *a*–*X* relationships with impure sodic clinopyroxene substitution can be
595 ideal or involve non-ideal mixing related to a miscibility gap between jadeite and
596 omphacite (*j*(o) (=X_{NaM2c} + X_{NaM2n})/2) at low *T* (<600°C: Newton & Smith, 1967; Liu
597 & Bohlen, 1995; Holland, 1983).

598 The omphacite–albite transition is sensitive to bulk fluid content. In fluid-
599 saturated equilibria, the albite-in reaction involves a transition of the trivariant gl–ep–
600 o–ab–pa–sph–H_2O field over a very narrow pressure interval (<0.5 kbar) at ~11 kbar
601 at 460°C (Figs 8b & 9a). The reaction occurs at slightly higher *P* than the breakdown
602 of glaucophane and paragonite to form additional albite together with chlorite and
603 stilpnomelane (10 kbar). The reaction is the expanded form of that emergent from gl +
604 pa = ab + chl in NMASH (Thompson et al., 1982; Holland & Ray, 1985; Guiraud et
605 al., 1990). An isothermal fluid-saturated decompression (*path A* in Fig. 9a) results in
606 only a small proportion of fluid during the omphacite–albite transition. The
607 progression to fluid undersaturated equilibria at pressures of 9–12 kbar involves a
608 change in the reaction assemblages related to albite growth. The multivariant change
609 involves jadeite and kyanite growth due to the consumption of paragonite and epidote
610 to accommodate excess alumina and soda (Fig. 9a). The multivariant fields of
611 coexisting omphacite and albite extend to higher-pressure (12.5 kbar) and expand
612 over a larger pressure interval of up to 4 kbar.
613 The decompression of assemblages preserved from zones 2b and 3 across the
614 blueschist– greenschist facies boundary is expected to trigger a local stage of internal
615 fluid generation (Fig. 8b: *cf.* Vry et al., 2010; Schorn, 2017; Chapman et al., 2022).
616 Depending on the amount of hydrous minerals (paragonite and glaucophane) retained
617 from the peak stage a small degree of back reaction is feasible. A P–M_{H2O}
618 pseudosection at *T* of 460°C posits the production of small portions of fluid (~0.5–1
619 mole %) at the intersection of the omphacite–albite trivariant field in zone 2b and 3
620 metasedimentary schists that have similar retained H_2O contents (Fig. 9a). Despite the
621 effects of differing peak-*P* and the consequences of initial retrograde cooling, limited
622 change is identified in the observed and inferred modes of hydrous minerals for the
623 metapelitic schists from zones 2b–4 (Fig. 11). A broad and indicative decompression

history can therefore be resolved using a fixed T of 460°C when most albite is growing. The paucity of albite in zone 4 schists is consistent with the limited availability of internal H_2O during exhumation (Fig. 11). Fluid undersaturated assemblages transect the albite–omphacite transition at marginally higher pressure but do not intersect kyanite growth (Fig. 9a). Localised domains of D_3 or D_4 shearing on the Peninsula do involve substantial external fluid ingress and the near-complete retrogression of peak assemblages.

Conjugate V–T path

Conjugate pseudosections incorporating V as a primary variable instead of P provide valuable information of the capacity to transform mineral assemblages (Fig. 10). The largest changes in assemblage V (and density) occur through low-variance equilibria (Fig. 10a: e.g. Powell et al., 2005; Etheridge et al., 2020; Chapman et al., 2022). The relationships make intuitive sense, with lower-pressure assemblages having greater V than high-pressure equilibria. During fluid-saturated prograde history mineral assemblages can progressively transform to new stable assemblages with differing volume upon crossing of the multivariant fields during temperature and pressure increases (Powell et al., 2019). Imposed deformation accommodates the volume change (Powell et al., 2005).

Substantial changes in V accompany fluid release events. The abrupt step-changes in V are best represented by the deflection of isobars transecting low-variance fields, like the lawsonite–epidote transition, that are narrow in P–T but expand in V–T pseudosection (Figs 10a & b). The transition from lawsonite-bearing to epidote-bearing equilibria, encompassing a total (solid plus fluid) V change on the order of 0.5 cm^3, though the solid volume may decrease (Fig. 10a). The volume expansion associated with the mineral dehydration can induce brittle or viscous deformation (e.g. veining: Etheridge et al., 2020; Chapman et al., 2022). However, the general

650 prograde trajectories of the Diahot metapelitic schist are unlikely to deviate
651 substantially on the *V*–*T* pseudosection of Figure 10a. In part, this is due to the large
652 temperature range traversed by the metamorphic sequence involving substantial
653 episodic fluid loss as well as the ability of syn-generational (S_1–S_2) deformation to
654 maintain the broad volume changes expected during mineral change (e.g. Carmichael,
655 1987; Powell et al., 2005).
656 The transition to fluid-undersaturation and patchy retrograde deformation–
657 metamorphism generates a transient mechanical scenario of relevance to the
658 application of the conjugate *V* pseudosection. In a fluid-absent and non-deforming
659 system it is harder for mineral assemblages to change volume as required for reactions
660 to occur (Powell et al., 2019). The reaction environment remains at constant volume
661 during cooling and decompression until it can adjust mechanically through the effects
662 of deformation or fluid ingress to enable further equilibration (e.g. Diener et al.,
663 2008).
664 The combination of fluid-undersaturation and a lack of penetrative
665 deformation until D_3 conditions (T = 450–480°C and P = 9–12 kbar) in the Diahot
666 metapelitic schists restricts any changes in volume for much of the exhumation path.
667 On the *V*–*T* pseudosection the retrograde trajectory (*path A*) involves cooling at
668 constant *V* through a series of metastable fields (Fig. 10b). The behaviour is distinct
669 from the fully equilibrated trajectory (*path B*), until the intersection of H_2O isopleths
670 of higher value, or the onset either deformation or fluid ingress (Fig. 10b). In the
671 Diahot metapelitic schists of zones 2b and 3, the constant volume boundary condition
672 is imposed on some scale until the omphacite–albite transition. The combination of
673 active deformation, small internal fluid production with or without fluid ingress
674 enables expansion (~1–1.42 cm^3) and reaction progression at the albite-in boundary,

675 and portions of the rock returning to near an equilibrated *V*–*T* path (red portions of
676 *path A*: Figs 10b & c).
677 *Volume change at omphacite–albite transition*
678 Volume change at the omphacite–albite transition is abrupt and large relative to the
679 pressure difference of the bounding univariant reactions (Fig. 10c). The transition
680 from sodic–calcic clinopyroxene- to albite-bearing equilibria involves a dilation of
681 between 0.5–0.6 cm^3 (Fig. 10c). There is less dilation in the transit of broad
682 multivariant fields. In a fluid-saturated system the omphacite–albite transition also
683 corresponds to the multivariant adjustment in paragonite, glaucophane and quartz
684 mode to facilitate albite growth and produce fluid. Decompressing Diahot metapelitic
685 schists are inferred to intersect this boundary and start retrogressing. The swap from
686 fluid undersaturated to saturated behaviour would accompany dilation. The extent of
687 change progressively increases (upwards of 1–2 cm^3) with the degree of indicative
688 fluid-undersaturation based on the specific case explored on Figure 9b. On the *V*–
689 M_{H2O} pseudosection this involves the progressive expansion of low-variance fields
690 involving co-existing albite and omphacite-equilibria with reduction in M_{H2O} (Fig.
691 9b).
692 The transect of metapelitic schists during decompression from 14 to 9 kbar
693 over the omphacite–albite transition can take a few forms (paths on Fig. 9). Albite
694 growth and reaction onset is predicted for many zone 2b and 3 schists due to a
695 transition back to fluid-saturation, in combination with D_3 deformation, the reaction
696 can accommodate some or all the volume change (~0.5–0.6 cm^3) at specific
697 dilatational microstructural sites. This behaviour will broadly follow *path A* on Figure
698 9b and depending on strain intensity can preserve omphacite with albite.
699 Progressively more fluid undersaturated rocks, like for example those from zone 4,
700 would intersect the omphacite–albite transition and lack the catalysing influence of

H_2O availability and would also require greater volume increases to enable any reaction completion (upwards of 1–2 cm^3). These schists have a restricted capacity for albite production to progress and are therefore predicted to support omphacite preservation in greater modes (*path B* on Fig. 9b). If at these *PT* conditions, high-strain deformation facilitates fluid ingress, then the near complete transformation of all omphacite to albite is considered likely and will induce a large volume increase as is observed in D_3 shear zones (*path C* on Fig. 9b).

DISCUSSION

Coexisting sodic–calcic clinopyroxene and albite

The consequences of dehydration of mineral assemblages during prograde and peak metamorphism necessitates fluid addition for any significant retrograde reaction to occur (e.g. Guiraud et al., 2001; White & Powell, 2002; Clarke et al., 2006). The extent of retrogression in any metamorphic cycle reflects the capacity of fluid to infiltrate a low-porosity rock. The effects of retrogression are commonly focused within highly strained metasedimentary rocks, likely due to their comparative ability to deform and generate porosity relative to that of more coherent metabasitic rocks (e.g. Heinrich, 1982; Rubie, 1990; Tenczer et al., 2006; Hobbs & Ord, 2010; Schorn, 2017). The preservation of abundant omphacite in metabasitic *versus* metapelitic assemblages in northern New Caledonia matches this generalization. Most strain related to the D_3 and D_4 events during terrane exhumation was focussed in the Diahot metasedimentary sequence, in the form of thrusting, folding and subsequent extensional faulting (Clarke et al., 1997). These are all structures which are associated with a localised increase in porosity suitable for fluid–rock interaction (e.g. Knipe & McCaig, 1994; Hobbs & Ord, 2010; Plümper et al., 2012; Jamtveit et al., 2016).

The distribution of prograde (S_2) sodic–calcic clinopyroxene in metapelitic assemblages in blueschist and eclogite from northern New Caledonia is inversely

727 correlated with the presence or absence of retrograde albite (Fig. 11e: Clarke et al.,
728 1997; Fitzherbert et al., 2005). Albite growth is associated with the breakdown of
729 primary sodic–calcic clinopyroxene, paragonite and glaucophane during retrograde
730 decompression (Fig. 8a: e.g. Holland & Ray, 1985; Carswell & Harley, 1990).
731 Omphacite survives as a matrix phase in domains that lack pervasive D_3 strain (Fig.
732 4c). Regions that experienced intense D_3 or D_4 shearing or folding have been
733 previously reported to contain only albite (Bell & Brothers, 1985). Nevertheless,
734 many samples on the Pam Peninsula have been shown to contain co-existing sodic–
735 calcic clinopyroxene, albite, and paragonite in apparent textural equilibrium (Figs 2–
736 7).

737 The coexistence of sodic–calcic clinopyroxene, albite and paragonite involves
738 specific microstructural form, associated with the development of S_3 folia during
739 arrested retrogression. Albite poikiloblasts formed late in the progressive D_3
740 exhumation event, overgrowing crenulated S_2 folia comprising paragonite- and
741 omphacite-bearing assemblages (e.g. Fig. 7). Omphacite and paragonite are rotated
742 and deformed by S_3 (Figs 6 & 7) consistent with them continuing to recrystallise
743 during initial albite growth (Fitzherbert et al., 2005). In domains of albite growth,
744 sodic–calcic clinopyroxene, paragonite and glaucophane survive either as inclusions
745 trails within albite or along grain margins as interfingered precursor S_2 or S_3 folia
746 (Figs 4a, 6 & 7).

747 Albite poikiloblasts formed preferentially in the hinge zones of the crenulation
748 generally lack substantial in-grain crystal distortion (<5°), exhibit growth-related
749 twins, and a grain form that is regularly pinned between bedding or S_3 folia partings
750 (Figs 2g & 7). Any significant crystal lattice bending is limited to grain margins
751 where the grain is pinned by S_3 folia (red arrow in Figs 6 & 7), plausibly
752 accommodating the force of grain growth (e.g. Bell et al., 1986; Maliva & Siever,

753 1988; Vernon, 1989). Irregular crystal outlines of albite trace its partial overgrowth of
754 precursor paragonite or sodic-calcic clinopyroxene. An epitaxial or topotaxial
755 relationship is retained to either omphacite/jadeite inclusions ($[010]_{ab}||[010]_{o}$) or
756 paragonite ($[010]_{ab}||[010]_{pa}$) consistent with crystallographic focussed growth (Figs 5–
757 7). Instances of D_3 albite growth within S_3 M-domains involve smaller highly
758 distorted grains, with a crystal habit that mimics precursor paragonite (Figs 4 & 6). It
759 remains difficult though, to resolve whether omphacite adjusted its composition at the
760 interface with the growing albite to retain some chemical or mechanical equilibrium
761 during the epitaxial/topotaxial replacement.

762 **Albite growth limited by fluid influx and strain partitioning**

763 The textural relationships of partial omphacite preservation in domains of varying D_3
764 strain are consistent with a deformation control in conjunction with limitations in the
765 extent of retrograde reaction due to H_2O buffering (Fig. 11). Restrictions on the
766 spatial distribution and completeness of albite growth in many samples away from
767 areas of high strain is consistent with a mostly local fluid source. Paragonite mode in
768 zones 2–4 metapelitic assemblages ranges from 6 to 15%. Together with contributions
769 from other hydrous minerals, the proportion of retained H_2O is predicted to be
770 between ~2–7 mole %, closely matching values posited by phase equilibria modelling
771 (4–7 mole %: Fig. 11).

772 The D_3 event in the Diahot terrane induced recrystallisation at lower blueschist
773 to greenschist facies conditions, associated with the development of albite,
774 clinozoisite, chlorite, and stilpnomelane (Fig. 8a: Yokoyama et al., 1985; Bell &
775 Brothers, 1985; Clarke et al., 1997; Fitzherbert et al., 2005). The retrograde path
776 inferred for the high-grade parts of the Eocene orogen does not intersect H_2O
777 isopleths of similar values to that of the peak conditions until the blueschist–
778 greenschist facies transition (Fig. 8b). The transition is accompanied by a small

779 production of fluid (~0.5–1 mole %), associated with the breakdown of paragonite,
780 glaucophane and omphacite to form albite, stilpnomelane and chlorite via a
781 multivariant reaction that is commonly inferred in blueschist terranes elsewhere (Fig.
782 9a: Holland & Ray, 1985; Koons & Thompson, 1985; Guiraud et al., 1990).
783 Internal fluid production during closed-system decompression should have
784 facilitated the breakdown of nearly all sodic–calcic clinopyroxene in the metapelitic
785 assemblages in NE New Caledonia. Complete recrystallization requires H_2O contents
786 of >6.5 mole % (Fig. 9). The breakdown posited by the phase equilibria modelling is
787 associated with extensive albite growth during decompression for peak assemblages
788 with retained whole rock H_2O contents between 5 and 7 mole % (Figs 8 & 9). Such
789 proportions match the abundances of hydrous phases observed in main rock types of
790 the Diahot terrane (Fig. 11). The relative proportions of albite, omphacite and
791 paragonite in the metapelitic assemblages from zones 2b, 3 and 4 highlight the effect
792 of subtle variations in the proportion of metastable hydrous phases (Fig. 11). These
793 would be compounded by additional adjustments in other hydrous phases found
794 within the rock like glaucophane, chlorite and mica. Most zone 3 and 4 metapelitic
795 assemblages have modes of paragonite, omphacite and albite in ratios consistent with
796 between 23 and 86% completion of the posited retrograde reactions (Fig. 11).
797 Reaction progress (ξ) in the zone 2 assemblages exceeds 90%, due to these rocks
798 having experienced a lower-grade metamorphic peak (*T)* and by them retaining higher
799 proportions of hydrous minerals (Fig. 11). Despite the availability of internally
800 derived fluid to 'trigger' reaction kinetics (Rubie, 1998), sodic–calcic clinopyroxene
801 survives.
802 Alternative interpretations of incomplete retrograde textures often invoke
803 limited diffusion scales and sluggish reaction kinetics due to lower temperatures of
804 retrograde processes after the cessation of deformation (e.g. Lasaga et al., 1986). The

805 reduction of diffusion scales with lower temperatures is known to contribute to the
806 formation of incomplete reaction textures involving coronae or symplectites (e.g.
807 White et al., 2008). However, the development of inclusions–host albite reaction
808 textures that are spatially focussed in microstructural domains of dilation such as
809 crenulation hinges implicate a restricted role for temperature-dependent diffusion on
810 the scale of equilibration (Figs. 5–7). This interpretation is supported by observed
811 pervasive albite growth in areas of high D_3 strain, the general paucity of delicate
812 coronae or symplectite reaction textures, and the local consumption of omphacite. The
813 ability of the microstructures of the reaction volume to deform at grain margins and
814 appears to be the controlling factor of albite growth and omphacite preservation even
815 after fluid was exhausted.

816 **Space-filling requirements of the new assemblage**

817 The incomplete breakdown of omphacite and paragonite must reflect additional
818 forcing mechanisms. The association of albite abundance and high D_3 strain is
819 consistent with a substantial contribution from deformation to reaction progress (ξ).
820 Albite poikiloblasts preferentially formed late in D_3 strain shadows or in hinge-zones
821 of F_3 crenulations (Figs 2 & 3). The spatial distribution of albite occurrences is
822 consistent with most (>83%) of its growth in microstructural domains of local
823 dilation, controlled by the heterogeneous accommodation of D_3 strain (Fig. 12: Bell,
824 1981; Maliva & Siever, 1988; Vernon, 1998; Worley et al., 1997; Williams et al.,
825 2001; Centrella, 2024). The limitation in albite growth appears to relate to the ability
826 to accommodate *P*–*V* work on the system (Powell et al., 2019).

827 Areas of the terrane that experienced low D_3 strain can be considered based on
828 a limiting condition of near constant volume associated with the retention of coarse-
829 grained, high-grade assemblages that developed during peak metamorphism. In the
830 absence of fluid-addition or deformation, the net effect is that for lower grade

831 conditions, equilibration volumes become progressively smaller, and mineral
832 assemblages become effectively 'locked' to change and thus more likely to be
833 preserved (Diener et al., 2008; Powell et al., 2019).
834 The recrystallization and reaction of metastable peak mineral assemblages at
835 different conditions occurs on the addition of fluid or with renewed deformation
836 (Guiraud et al., 2001; Chapman et al., 2019a, b). The transition across the blueschist–
837 greenschist boundary during cooling produces small amounts of H_2O in association
838 with paragonite and omphacite breakdown (Fig. 11c). Until the intersection of this
839 reaction the peak mineral assemblage has remained at a near constant volume except
840 for some minor elastic relaxation (*path A* on Fig. 10b). For reaction progress to occur,
841 a given rock environment must deform to accommodate necessary local volume
842 increases that can be on the order of~1–1.42 cm^3associated with changing molar
843 volumes at the albite–omphacite transition (Holland, 1980; Powell et al., 2005).
844 Effectively, the space filling requirements of the new assemblage enable albite to
845 preferentially form in microstructural areas of dynamic dilation, due to its lower
846 density that requires more space for growth (Fig. 12). If external fluid infiltration
847 occurs, progressive equilibration could be expected to obliterate the peak
848 metamorphic microstructure along the inferred retrograde path, which is the case for
849 much of the highly strained Diahot terrane (Figs 3 & S1: Bell & Brothers, 1985;
850 Clarke et al., 1997; Fitzherbert et al., 2005). In doing so, the given metastable
851 assemblage will efficiently convert to the new mineral assemblages due to the larger
852 equilibration volumes that reflect the local ambient *P–T–V* conditions (*path C* on Fig.
853 9b). The greatest reaction progress is typically focussed along shear zones that act as
854 effective strain loci, dilation sites and fluid conduits, contributing to a retrogression–
855 weakening–porosity feedback loop (e.g. Rubie, 1986; Hobbs et al., 2010; Plümper et
856 al., 2012; Jamtveit et al., 2016 Chapman et al., 2022). The abundance of albite in

857 regions of intense D_3 strain in the Diahot terrane is consistent with such a feedback
858 relationship involving dynamic dilatancy formation during terrane exhumation (Fig.
859 12).

860 The lack of pervasive high strain experienced by many of the metapelitic
861 schists in the Diahot Terrane means any volume change is limited to that which can
862 be accommodated by a given rock's environment. The extent of volume change
863 related to partial retrogression accompanying internal fluid production is inferred to
864 be between 0.18–0.81 cm^3, which matches the observed changes in mineral modes
865 (0.15–0.80 cm^3) in metapelitic samples from zone 3 with co-existing sodic–calcic
866 clinopyroxene and albite (*path A* on Fig. 9b). Greater change is limited by the lack of
867 physical volume adjustment available to create space for the retrograde mineral
868 assemblage. Overcoming this imposed space-filling requirement of the assemblage
869 requires the generation of self-stress from the mineral reaction (e.g. Correns, 1949;
870 Carmichael, 1987; Powell et al., 2019; Chapman et al., 2019a, 2022; Centrella, 2024).

871 During hydration reaction progress, any volume change commonly involves
872 fracturing to generate porosity and enable fluid flow, that in turn can facilitate
873 reactions in a cyclical manner (Plümper et al., 2012; Okamoto & Shimizu, 2015). The
874 combination of a high confining *P* and limited internal fluid production would have
875 likely restricted any substantial fracturing in the crenulated metapelitic schists. Any
876 generated stress appears to have mostly been accommodated via elastic grain
877 boundary adjustment (e.g. Wintsch et al., 2024) and with some lattice distortion of
878 growing crystals to fill open spaces. This suggests all fluid was utilised in the
879 retrograde reactions, limiting any changes in pore-fluid to drive the formation of veins
880 to accommodate the increase in *V* and produce an overpressure or drive substantial
881 open mass transfer (Etheridge et al., 2020; Chapman et al., 2022). A greater
882 abundance of late-stage albite veins coincident with high-strain D_3 structures is

consistent with greater fluid flux (higher-porosity) associated with more complete reaction progress. Advective sodium mobility in these locations may in part contribute to greater abundances of albite and departures from an idealised volume constraint for a now open system (e.g. Korzhinskii, 1965; Miller & Cartwright, 2006; Diener et al., 2008; Powell et al., 2019). In general, the combined effects of a buffered internal fluid content and a volume or mechanical limitation can account for the paradoxical occurrence reactants of sodic–calcic clinopyroxene and products of albite.

Chemical–mechanical feedback

The contributions of both deformation and fluid migration in rocks undergoing metamorphism induce complicated feedbacks (Hobbs et al., 2010; Okamoto & Shimizu, 2015; Chapman et al., 2019b). As a rock passes through its inferred prograde and retrograde *PT* history it evolves via thermal, mechanical and chemical dissipative processes (Powell et al., 2019). The extent of change of a mineral assemblage will depend critically on the rates of the various dissipative processes that contribute to establishing an equilibrium as well as those that contribute to its microstructural form (Hobbs & Ord, 2016; Powell et al., 2019).

Instances of focussed mineral nucleation, such for albite in the Diahot terrane schists, in low-strain sites or boundaries like the hinge of a continuous crenulation cleavage, has been related to mixed mechanical–chemical gradients (Bell et al., 1986; Worley et al.,1997; Williams et al., 2001). Differential responses to strain imposed on sheared (coaxial) phyllosilicate-rich (M-domains) limbs versus that imposed on shortened (non-coaxial) quartz-rich hinge (Q-domains) zones are inferred to generate strain energy gradients that would influence sites of mineral growth (e.g. Bell et al., 1986). The tightening of the microfolds progressively exaggerates the heterogeneous strain partitioning between these domains. Dissolution-precipitation creep in mica, amphibole, and clinozoisite in sheared domains provide the mass to be transferred and

909 precipitated at sites (Q-domains) of lower mean stress to form dilating albite (Marlow
910 & Etheridge, 1977; Bell et al., 1986; Mancktelow, 1994; Vernon, 1998). These
911 features implicate the mobility of Na and Al on a scale of the crenulation spacing
912 aided by fluid transport in an effectively closed system on the scale of the rock
913 (Etheridge et al., 1983; Worley et al., 1997; Powell et al., 2019; Schorn, 2022).
914 Space filling requirements of crystal growth are inherently influenced by the
915 nature of the heterogeneous strain. Rock domains of higher strain energy are
916 considered to result in microstructural locations of distinct nucleation potential that
917 help to overcome a nucleation barrier (e.g. Gaidies, 2017; George & Gaidies, 2020
918 and thus enable reaction progression (Hobbs et al., 2019). These reaction sites can
919 then drive differential diffusive adjustment to new imposed chemical potential
920 gradients (e.g. White et al., 2008; Powell et al., 2019), plausibly aided by fluid
921 migration along gradients in pore-fluid pressure, mostly likely along elastic grain
922 boundaries (Etheridge et al., 1983; Chapman et al., 2022).
923 In circumstances of preserved porphyroblast growth, like that of albite in the
924 Diahot blueschists, resolving any former gradient in strain energy is difficult, on
925 account of the combined effects of plastic recovery and crystal interfacial
926 adjustments. Qualitative dislocation densities directly related to crystal lattice
927 distortion in quartz and omphacite crystals are in general highest in grains adjacent to
928 the shearing M-domains relative to the hinge (Fig. 7). Preserved inclusions of
929 omphacite and quartz in albite poikiloblasts retain crystal distortion and inherited
930 crystallographic preferred orientations consistent with stored, and partially recovered,
931 dislocation derived strain energy (Fig. 7: e.g. Wheeler et al., 2024). The
932 predominance of dissolution-precipitation creep in mica and amphibole implies that
933 their energy dissipation would have been accommodated by the interfacial movement
934 of the crystal boundaries (Drury & Urai, 1990). The coincidence of albite

crystallographic axes to omphacite/jadeite or paragonite is consistent with epitaxial or topotaxial crystallisation helping to overcome the energetic dissipation constraints of dislocations, similar to predictions of garnet nucleation (Fig. 6: George & Gaidies, 2020). Although, our observations suggests that stored dislocation energy also appears to have played a role, it remains difficult to quantify the absolute influence on the kinetics of mineral nucleation. Nevertheless, the results show that the contribution of volume changes imposed by the reaction and strain gradients in the developing microstructure dictate the ability to substantially grow any formed nucleus.

The inhibited reaction between sodic–calcic clinopyroxene, paragonite and albite implies metamorphic inefficiencies in terms of crystal growth. Any growth of albite poikiloblasts must initially satisfy the space filling requirements of the evolving reacting–deforming microstructure (Hobbs et al., 2019). The retention of fine-scale microstructures of the precursor phases in the form of crystallography, aligned inclusions trails and irregular growth morphologies, implies growth was initially attempting to retain some volume of the reactants. In fact, in domains undergoing shearing with limited volume change albite has grown in a manner that retains the volume of precursor phases (Fig. 7).

The substantial increase of the solid volume of the reaction necessitates strain adjustment for any substantive growth and potential reaction completion (Figs 11 & 12). This change in growth behaviour is an attempt to retain deformation compatibility between the porphyroblasts and the surrounding matrix (Hobbs et al., 2019). In conjunction with requirements to minimise interfacial energy, mutual impingement of the often-idiomorphic faces of albite with surrounding matrix phases may contribute to the indentation and crystal distortion observed at its grain edge (Fig. 6). Localised lattice distortion in the rims of albite porphyroblasts pinned against S_3 folia may be consistent with accommodation of some of this stress via a ‘force of

961 crystallisation' (Vernon, 1989). In either case, the restricted dilatational sites for albite
962 growth arrested the reaction and enabled the metastable preservation of precursor
963 sodic–calcic clinopyroxene and paragonite to low-pressure conditions (Fig. 12).

964 **CONCLUSIONS**

965 Jadeite and omphacite coexisting with albite and paragonite in blueschist and eclogite
966 of NE New Caledonia relate to limited internal fluid production and a lack of
967 deformation to accommodate large volume change associated with reaction.
968 Equilibrium volumes adjust when mineral assemblages become fluid-absent near the
969 metamorphic peak and active fluid-present deformation or annealing ceases. The
970 localised breakdown of paragonite is predicted to provide sufficient fluid to initiate
971 albite growth, though its expansion during crystallisation is inhibited by a lack of
972 penetrative deformation, effectively protecting metastable sodic–calcic
973 clinopyroxene. Albite growth is restricted to microstructural domains involving
974 dynamic dilation. Domains of high D_3 and D_4 shear facilitate volume accommodation,
975 inducing a dramatic increase in the size of the equilibration volume and the complete
976 breakdown of sodic–calcic clinopyroxene to form albite. The space-filling
977 requirements of equilibrium mineral assemblages warrants careful consideration for
978 decompression-induced retrograde reactions. Precursor assemblages commonly partly
979 survive in domains that escape significant hydration and/or deformation in most
980 metamorphic terranes.

981

982

983

984 **REFERENCES**

985 Aitchison, J.C., Clarke, G.L., Cluzel, D. & Meffre, S. (1995). Eocene arc-continent
986 collision in New Caledonia and implications for regional SW Pacific tectonic
987 evolution. *Geology* **23**, 161–164.
988 Baldwin, S.L., Rawling, T., Fitzgerald, P.G. (2007). Thermochronology of the New
989 Caledonian high-pressure terrane: implications for middle Tertiary plate
990 boundary processes in the southwest Pacific. In: Cloos, M., Carlson, W.D.,
991 Gilbert, M.C., Liou, J.G., Sorensen, S.S. (Eds.), *Convergent Margin Terranes*
992 *and Associated Regions: A Tribute to W.G. Ernst*. Geological Society of
993 America Special Paper, 117–134.
994 Bell, T. H. (1981). Foliation development – the contribution, geometry and
995 significance of progressive, bulk, inhomogeneous shortening. *Tectonophysics*,
996 **75**, 273–296.
997 Bell, T. H. & Brothers, R. N. (1985). Development of P–T prograde and P-retrograde,
998 T-prograde isogradic surfaces during blueschist to eclogite regional
999 deformation/metamorphism in New Caledonia, as indicated by progressively
1000 developed porphyroblast microstructures. *Journal of Metamorphic Geology*, **3**,
1001 59–78.
1002 Bell, T., Rubenach, M., & Fleming, P. (1986). Porphyroblast nucleation, growth and
1003 dissolution in regional metamorphic rocks as a function of deformation
1004 partitioning during foliation development. *Journal of Metamorphic Geology,*
1005 **4**, 37–67.
1006 Black, P. M. (1974). Mineralogy of New Caledonian metamorphic rocks III.
1007 Pyroxenes, and major element partitioning between coexisting pyroxenes,
1008 amphiboles and garnets from the Ouégoa district. *Contributions to Mineralogy*
1009 *and Petrology*, **45**, 281–288.

1010 Black, P.M. (1977). Regional high-pressure metamorphism in New Caledonia: phase
1011 equilibria in the Ouégoa district. *Tectonophysics,* **43**, 89–107.
1012 Black, P.M., Brothers, R.N. & Yokoyama, K. (1988). Mineral paragenesis in eclogite-
1013 facies meta-acidites in northern New Caledonia. In: Smith, D.C. (ed.),
1014 *Eclogites and Eclogite-Facies Rocks*. Elsevier, Amsterdam, pp. 271–289.
1015 Brothers, R.N. (1974). High-pressure schists in northern New Caledonia.
1016 *Contributions to Mineralogy and Petrology*, **46**, 109–127.
1017 Carmichael, D. M. (1987). Induced stress and secondary mass transfer:
1018 thermodynamic basis for the tendency toward constant-volume constraint in
1019 diffusion metasomatism. In: Helgeson, H.C. (Ed.), Chemical Transport in
1020 Metasomatic Processes. Springer, Netherlands, Dordrecht, pp. 239–264.
1021 Carson, C.J., Powell, R. & Clarke, G.L., 1999. Calculated mineral equilibria for
1022 eclogites in $CaO–Na_2O–FeO–MgO–Al_2O_3–SiO_2–H_2O$: application to the
1023 Pouébo Terrane, Pam Peninsula, New Caledonia. *Journal of Metamorphic*
1024 *Geology*, **17**, 9–24.
1025 Carson, C.J., Clarke, G.L. & Powell, R. (2000). Hydration of eclogite from the Pam
1026 Peninsula, New Caledonia. *Journal of Metamorphic Geology*, **18**, 79–90.
1027 Carswell, D. A. & Harley, S. (1990). Experimental studies on the stability of eclogite
1028 facies mineral parageneses. In Carswell, D. A. (Ed.) *Eclogite Facies Rocks*,
1029 Blackie, London, 53–83.
1030 Centrella, S. (2024). A new insight into metasomatism through mass-density-solid
1031 volume variation maps. *Geochemistry*, **84**, 126043.
1032 Chapman, T., Clarke, G. L., Piazolo, S., Robbins, V. A., Trimby, P. W. (2019a).
1033 Grain-scale dependency of metamorphic reaction on crystal plastic strain.
1034 *Journal of Metamorphic Geology*, **37**, 1021–1036.

1035 Chapman, T., Clarke, G. L., Piazolo, S., Daczko, N. R. (2019b). Inefficient high-
1036 temperature metamorphism in orthogneiss. *American Mineralogist*, **104**, 17–
1037 30.
1038 Chapman, T., Clarke, G. L., Daczko, N. R. (2019c). The role of buoyancy in the fate
1039 of ultra-high-pressure eclogite. *Scientific Reports*, DOI: 10.1038/s41598-019-
1040 56475-y.
1041 Chapman, T. & Clarke, G. L. (2021). Cryptic evidence for the former presence of
1042 lawsonite in blueschist and eclogite. *Journal of Metamorphic Geology*, doi:
1043 10.1111/jmg.12578.
1044 Chapman, T., Milan, L. A. & Vry, J. (2022). The role of metamorphic fluid in
1045 tectonic tremor along the Alpine Fault, New Zealand. *Geophysical Research*
1046 *Letters*, e2021GL096415.
1047 Clarke, G.L., Aitchison, J.C. & Cluzel, D. (1997). Eclogites and blueschists of the
1048 Pam Peninsula, NE New Caledonia: a reappraisal. *Journal of Petrology*, **38**,
1049 843–876.
1050 Clarke, G. L., Daczko, N. R., Noccolds, C. (2001). A method for applying matrix
1051 corrections to X-ray intensity maps using the Bence-Albee algorithm and
1052 Matlab. *Journal of Metamorphic Geology*, **19**, 653–662.
1053 Clarke, G. L., Powell, R., Fitzherbert, J. A. (2006). The lawsonite paradox: a
1054 comparison of field evidence and mineral equilibria modelling. *Journal of*
1055 *Metamorphic Geology*, **24**, 715–725.
1056 Cluzel, D., Aitchison, J., Clarke, G. L., Meffre, S., Picard, C. (1994). Point de vue sur
1057 l'évolution tectonique et géodynamique de la Nouvelle-Calédonie (Pacifique,
1058 France). *Comptes Rendus Hebdomadaires des Séances de l'Académie des*
1059 *Sciences, Série II*, **321**, 57–64.

1060 Correns, C. W. (1949). Growth and dissolution of crystals under linear pressure.
1061 *Discussions of the Faraday Society*, **5**, 267–271.
1062 Diener, J. F. A., White, R. W., Powell, R. (2008). Granulite facies metamorphism and
1063 subsolidus fluid-absent reworking, Strangways Range, Arunta Block, central
1064 Australia. *Journal of Metamorphic Geology*, **26**, 603–622.
1065 Drury, M., & Urai, J. (1990). Deformation-related recrystallisation processes.
1066 *Tectonophysics*, **172**, 235–253.
1067 Etheridge, M. A., Wall, V. J., Vernon, R. H. (1983). The role of the fluid phase during
1068 regional metamorphism and deformation. *Journal of Metamorphic Geology*, **1**,
1069 205–226.
1070 Etheridge, M. A., Daczko, N. R., Chapman, T. & Stuart, C. A. (2020). Mechanisms of
1071 melt extraction during lower crustal partial melting. *Journal of Metamorphic*
1072 *Geology*, DOI: 10.1111/jmg.12561.
1073 Evans, K.A. & Powell, R. (2015). The effect of subduction on the sulphur, carbon and
1074 redox budget of lithospheric mantle. *Journal of Metamorphic Geology*, **33**,
1075 649–670.
1076 Fitzherbert, J. A. (2002). Eocene high-P metamorphism in NE New Caledonia.
1077 Unpublished PhD Thesis, The University of Sydney, pp 201.
1078 Fitzherbert, J.A., Clarke, G.L., Powell, R. (2003). Lawsonite–omphacite bearing
1079 metabasites of the Pam Peninsula, NE New Caledonia: evidence for disrupted
1080 blueschist to eclogite facies conditions. *Journal of Petrology*, **44**, 1805–1831.
1081 Fitzherbert, J. A. Clarke, G. L., Marmot, B. & Powell, R. (2004). The origin and *P–T*
1082 evolution of peridotites and serpentinites of NE New Caledonia: prograde
1083 interaction between continental margin and the mantle wedge. *Journal of*
1084 *Metamorphic Geology*, **22**, 327–344.

1085 Fitzherbert, J.A., Clarke, G.L., Powell, R. (2005). Preferential retrogression of high-P
1086 metasediments and the preservation of blueschist to eclogite facies metabasite
1087 during exhumation, Diahot terrane, NE New Caledonia. *Lithos*, **83**, 67–96.
1088 Früh-Green, G. (1994). Interdependence of deformation, fluid infiltration and reaction
1089 progress in eclogitic metagranitoids (Sesia Zone, Western Alps). *Journal of*
1090 *Metamorphic Geology*, **12**, 327–343.
1091 Gaidies, F. (2017). *Nucleation in geological materials*. EMU Notes in Mineralogy.
1092 European Mineralogical Union, book section 11.
1093 George, F. & Gaidies, F. (2020). Simultaneous operation of opposing reaction
1094 mechanisms: The influence of matrix heterogeneity on post-kinematic garnet
1095 crystallization in an inverted metamorphic sequence. *Journal of Metamorphic*
1096 *Geology*, doi: 10.1111/jmg.12539.
1097 Ghent, E. D., Roddick, J. C. & Black, P. M. (1994). $^{40}Ar/^{39}Ar$ dating of white micas
1098 from the epidote to omphacite zones, northern New Caledonia: tectonic
1099 implications. *Canadian Journal of Earth Sciences*, **31**, 995–1001.
1100 Guiraud, M., Holland, T. J. B. & Powell, R. (1990). Calculated mineral equilibria in
1101 the greenschist–blueschist-eclogite facies in Na_2O–FeO–MgO–$Al2O_3$–SiO_2–
1102 H_2O. *Contributions to mineralogy and Petrology*, **104**, 85–98.
1103 Guiraud, M., Powell, R., Rebay, G. (2001). H_2O in metamorphism and unexpected
1104 behaviour in the preservation of metamorphic mineral assemblages. *Journal of*
1105 *Metamorphic Geology*, **19**, 445–454.
1106 Green, E. C. R., White, R. W., Diener, J. F. A., Powell, R., Holland, T. B. J., Palin, R.
1107 M. (2016). Activity–composition relations for the calculations of partial
1108 melting equilibria for metabasic rocks. *Journal of Metamorphic Geology*, **34**,
1109 845–869.

1110 Heinrich, C. A. (1982). Kyanite-eclogite to amphibolite facies evolution of hydrous
1111 mafic and pelitic rocks, Adula Nappe, Central Alps. *Contributions to*
1112 *Mineralogy and Petrology*, **81**, 30–38.
1113 Hobbs, B. E., Ord, A., Spalla, M. I., Gosso, G. & Zucali, M. (2010). The interaction
1114 of deformation and metamorphic reactions. *Geological Society, London*
1115 *Special Publications*, **332**, 189–223.
1116 Hobbs, B. E. & Ord, A. (2016). Does non-hydrostatic stress influence the equilibrium
1117 of metamorphic reactions? *Earth Science Reviews*, **163**, 190–233.
1118 Hobbs, B. E., Ord, A., Ulrich, S., & Schulman, K. (2019). Rheology of mixed
1119 deformation mechanisms and mineral phase assemblages. *Journal of*
1120 *Structural Geology*, **129**, 103891.
1121 Holland, T. J. B. (1980). The reaction albite = jadeite + quartz determined
1122 experimentally in the range 600–1200°C. *American Mineralogist*, **65**, 129–
1123 134.
1124 Holland, T. J. B. (1983). The experimental determination of activities in disordered
1125 and short-range ordered jadeitic pyroxenes. *Contributions to Mineralogy and*
1126 *Petrology*, **82**, 214–220.
1127 Holland, T. J. B. & Ray, N. J. (1985). Glaucophane and pyroxene breakdown
1128 reactions in the Pennine units of the Eastern Alps. *Journal of Metamorphic*
1129 *Geology*, **3**, 417–438.
1130 Holland, T. J. B. & Powell, R. (2011). An improved and extended internally
1131 consistent thermodynamic dataset for phases of petrological interest, involving
1132 a new equation of state for solids. *Journal of Metamorphic Geology,* **29**, 333–
1133 383.

1134 Holland, T. J. B., Green, E. C. R., Powell, R. (2021). A thermodynamic model for
1135 feldspar in $KAlSi_3O_8$–$NaAlSi_3O_8$–$CaAlSi_3O_8$ for mineral equilibrium
1136 calculations. *Journal of Metamorphic Geology*, 40, 587–600.
1137 Jamtveit, B., Austrheim, H., Putnis, A. (2016). Disequilibrium metamorphism of
1138 stressed lithosphere. *Earth-Science Reviews*, **154**, 1–13.
1139 Johannes, W., Bell, P. M., Boettcher, A. L., Chipman, D. W., Hays, J. F., Mao, H. K.,
1140 Newton, R. C., Seifert, F. (1971). An inter-laboratory comparison of piston-
1141 cylinder pressure calibration using the albite-breakdown reaction.
1142 *Contributions to Mineralogy and Petrology*, **32**, 24–38.
1143 Knipe, R. J. & McCaig, A. M. (1994). Microstructural and microchemical
1144 consquences of fluid flow in deforming rocks. *Geological Society, London,*
1145 *Special Publications*, **78**, 99–111.
1146 Koons, P. O., Rubie, D. C. & Frueh-Green, G. (1987). The effects of disequilibria and
1147 deformation on the mineralogical evolution of quartz diorite during
1148 metamorphism in the eclogite facies. *Journal of Petrology*, **28**, 679–700.
1149 Koons, P. O. & Thompson, A. B. (1985). Non-mafic rocks in the greenschist,
1150 blueschist and eclogite facies. *Chemical Geology*, **50**, 3–30.
1151 Korzhinskii, D. S. (1965). The theory of systems with perfectly mobile components
1152 and processes of mineral formation. *American Journal of Science*, **263**, 193–
1153 205.
1154 Lasaga, A. C. (1986). Metamorphic reaction rate laws and development of isograds.
1155 *Mineralogical Magazine*, **50**, 359–373.
1156 Leake, B. E., Woolley, A. R., Arps, C. E. S., Birch, M. C., Grice. J. D., Hawthorne, F.
1157 C., Kato, A., Kisch, H. J., Krivovichiev, V. G., Linthout, K., Laird, J.,
1158 Mandarino, J. A., Maresch, W. V., Nickel, E. H., Rock, N. M. S., Schumacher,
1159 J.C., Smith, D. C., Stephenson, N. C. N., Ungaretti, L., Whittaker, E. J. W. &

1160 Youzhi, G. (1997). Nomenclature of amphiboles: report of the subcommittee
1161 on amphiboles of the international mineralogical association, commission on
1162 new minerals and mineral names. *The Canadian Mineralogist*, **35**, 219–246.
1163 Liu, J. & Bohlen, S. R. (1995). Mixing properties and stability of jadeite-acmite
1164 pyroxene in the presence of albite and quartz. *Contributions to Mineralogy*
1165 *and Petrology*, **119**, 433–440.
1166 Maliva, R. G. & Siever, R. (1988). Diagenetic replacement controlled by force of
1167 crystallization. *Geology*, **16**, 688–691.
1168 Mancktelow, N. S. (1994). On volume change and mass transport during development
1169 of crenulation cleavage. *Journal of Structural Geology*, **16**, 1217–1231.
1170 Marlow, P. C., & Etheridge, M. A. (1977). Development of a layered crenulation
1171 cleavage in mica schists of the Kanmantoo Group near Macclesfield, South
1172 Australia. *Geological Society of America Bulletin*, **88**, 873–882.
1173 Marmo, B.A., Clarke, G.L. & Powell, R. (2002). Fractionation of bulk rock
1174 composition due to porphyroblast growth: effects on eclogite facies mineral
1175 equilibria, Pam Peninsula, New Caledonia. *Journal of Metamorphic Geology*,
1176 **20**, 151–165.
1177 Maurizot, P., Eberlé, J-M., Habault, C. & Tessarollo, C. (1989). Carte geologique à
1178 l'échelle du 1/50000, feuille Pam-Ouégoa: Paris, Bureau des recherches
1179 Geoloiques et Minieres, Map sheet and explanatory notes, 81 pp.
1180 Maurizot, P. (2001). Carte géologique de la Nouvelle-Caledonie, 1:1000000. BRGM-
1181 DIMENC.
1182 Miller, J. A., & Cartwright, I. (2006). Albite vein formation during exhumation of
1183 high-pressure terranes: a case study from alpine Corsica. *Journal of*
1184 *Metamorphic Geology*, **24**, 409–428.

1185 Miyano, T. & Klein, C. (1989). Phase equilibria in the system K_2O–FeO–MgO–
1186 Al_2O_3–SiO_2–H_2O–CO_2 and the stability limit of stilpnomelane in
1187 metamorphosed Precambrian iron formations. *Contributions to Mineralogy*
1188 *and Petrology*, **102**, 478–491.
1189 Morimoto, N. (1989). Nomenclature of pyroxenes. *Canadian Mineralogist*, **27**, 143–
1190 156.
1191 Newton, R. C. & Smith, J. V. (1967). Investigations concerning the breakdown of
1192 albite at depth in the earth. *Journal of Geology*, **75**, 268–286.
1193 Okamoto, A., Shimizu, H. (2015). Contrasting fracture pattersn induced by volume-
1194 increasing and decreasing reactions: implications for the progress of
1195 metamorphic reactions. *Earth and Planetary Science Letters*, **417**, 9–18.
1196 Palin, R. M., Reuber, G.S., White, R. W., Kau, B. J. P., Weller, O. M. (2017).
1197 Subduction metamorphism in the Himalayan ultrahigh-pressure Tso Morari
1198 massif: an integrated geodynamic and petrological modelling approach. *Earth*
1199 *and Planetary Science Letters*, **467**, 108–119.
1200 Paris, J. P. (1981). Géologie de la Nouvelle-Calédonie: Bureau des Recherches
1201 Géologiques et Minières Mémoir, 113, 279 pp.
1202 Piazolo, S., Bestmann, M., Prior, D. J., Spiers, C. J. (2006). Temperature dependent
1203 grain boundary migration in deformed-then-annealed material: observations
1204 from experimentally deformed synthetic rocksalt. Tectonophysics, **427**, 55–71.
1205 Pirard, C. & Spandler, C. (2017). The zircon record of high-pressure metasedimentary
1206 rocks of New Caledonia: implications for regional tectonics of the south-west
1207 Pacific. *Gondwana Research*, **46**, 79–94.
1208 Plümper, O., Røyne, A., Magraso, A., Jamtveit, B. (2012). The interface-scale
1209 mechanisms of reaction-induced fracturing during serpentinization. *Geology*,
1210 **40**, 1103–1106.

1211 Powell, R. (1983). Fluids and melting under upper amphibolite facies conditions.
1212 *Journal of The Geological Society, London*, **140**, 629–633.
1213 Powell, R. & Holland, T. J. B. (1988). An internally consistent dataset with
1214 uncertainties and correlations: 3. Applications to geobarometry, worked
1215 examples and a computer program. *Journal of Metamorphic Geology,* **6**, 173–
1216 204.
1217 Powell, R., Guirand, M., White, R. W. (2005). Truth and beauty in metamorphic
1218 phase equilibria: conjugate variables and phase diagrams. *The Canadian*
1219 *Mineralogist*, **43**, 21–33.
1220 Powell, R., Evans, K. A., Green, E. C. R., White, R. W. (2019). The truth and beauty
1221 of chemical potentials. *Journal of Metamorphic Geology*, doi:
1222 10.1111/jmg.12484.
1223 Proyer, A. (2003). The preservation of high-pressure rocks during exhumation:
1224 metagranites and metapelites. *Lithos*, **70**, 183–194.
1225 Rawling, T.J. & Lister, G.S. (2002). Large-scale structure of the eclogite-blueschist
1226 belt of New Caledonia. *Journal of Structural Geology*, **24**, 1239–1258.
1227 Rebay, G. Powell, R. & Holland, T. J. B. (2022). Calculated phase equilibria for high-
1228 pressure serpentinites and compositionally related rocks close to the MgO–
1229 Al_2O_3–SiO_2–H_2O (MASH) system. *Journal of Metamorphic Geology*, doi:
1230 10.1111/jmg12663.
1231 Robinson, P., Spear, F. S., Schumacher, J. C., Laird, J., Klein, C., Evans, B. W. &
1232 Doolan, B. L. (1982). Phase relations of metamorphic amphiboles: natural
1233 occurrence and theory. In: Veblen, D. R. & Ribbe, P. H. (eds) Amphiboles:
1234 Petrology and Experimental Phase Relations. Mineralogical Society of
1235 America, Reviews in Mineralogy 9B, 1–227.

1236 Rogowitz, A. & Huet, B. (2021). Evolution of fluid pathways during eclogitization
1237 and their impact on formation and deformation of eclogite. A microstructural
1238 and petrological investigation at the type locality (Koralpe, Eastern Alps,
1239 Austria). *Tectonophysics*, **819**, 229079.
1240 Rubie, D. C. (1986). The catalysis of mineral reactions by water and restrictions on
1241 the presence of aqueous fluid during metamorphism. *Mineralogical Magazine*,
1242 **50**, 399–415.
1243 Rubie, D. C. (1990). Role of kinetics in the formation and preservation of eclogites. In
1244 Carswell, D. A. (Ed.) *Eclogite facies rocks*, Blackie, London, 111–140.
1245 Rubie, D. C. (1998). Disequilibrium during metamorphism: the role of nucleation
1246 kinetics. In Treloar, P. J. & O'Brien, P. J. (Eds) *What drives metamorphism*
1247 *and metamorphic reactions?* Geological Society, London Special
1248 Publications, **138**, 199–124.
1249 Schorn, S. (2017). Dehydration of metapelites during high-*P* metamorphism: the
1250 coupling between fluid sources and fluid sinks. *Journal of Metamorphic*
1251 *Geology*, **36**, 369–391.
1252 Schorn, S. (2022). Self-induced incipient 'eclogitization' of metagranitoids at closed-
1253 system conditions. *Journal of Metamorphic Geology*, doi: 10.1111/jmg.12665.
1254 Spandler, C. & Rubatto, D. (2005). Late Cretaceous–Tertiary tectonics of the
1255 southwest Pacific: Insights from U-Pb sensitive, high-resolution ion
1256 microprobe (SHRIMP) dating of eclogite facies rocks from New Caledonia.
1257 *Tectonics*, 24, doi:10.1029/2004TC001709.
1258 Spandler, C., Hermann, J., Faure, K., Mavorogenes, J. A., Arculus, R. J. (2008). The
1259 importance of talc and chlorite 'hybrid' rocks for volatile recycling through
1260 subduction zones; evidence from the high-pressure subduction mélange of
1261 New Caledonia. *Contributions to Mineralogy and Petrology*, **155**, 181–198.

1262 Taetz, S., John, T., Bröcker, M., Spandler, C., Stracke, A. (2018). Fast intraslab fluid-
1263 flow events linked to pulses of high pore fluid pressure at subducted plate
1264 interface. *Earth and Planetary Science Letters*, **482**, 33–43.
1265 Taetz, S., Scherer, E. E., Bröcker, M., Spandler, C., John, T. (2021). Petrological and
1266 Lu–Hf age constraints for eclogitic rocks from the Pam Peninsula, New
1267 Caledonia. *Lithos*, **388–389**, 106073.
1268 Tenczer, V., Powell, R. & Stüwe, K. (2006). Evolution of H_2O content in a
1269 polymetamorphic terrane: the Plattengneiss shear zone (Koralpe, Austria).
1270 *Journal of Metamorphic Geology*, **24**, 281–295.
1271 Thompson, J. B. (1955). The thermodynamic basis for the mineral facies concept.
1272 *American Journal of Science*, **253**, 65–103.
1273 Thompson, J. B., Larid, J. & Thompson, A. B. (1982). Reactions in amphibolite,
1274 greenschist and blueschist. *Journal of Petrology*, **23**, 1–27.
1275 Thompson, A. B. (1983). Fluid-absent metamorphism. *Journal of the Geological*
1276 *Society of London*, **140**, 533–547.
1277 Vernon, R. H. (1989). Porphyroblast-matrix microstructural relationships: recent
1278 approaches and problems. In Daly, J. S., Cliff, R. A. & Yardley, B. W. D.
1279 (Eds) 1989, *Evolution of Metamorphic Belts*, Geological Society Special
1280 Publication, **43**, 83-102.
1281 Vernon, R. H. (1998). Chemical and volume changes during deformation and
1282 prograde metamorphism of sediments. In Treloar, P. J. & O'Brien, P. J. (Eds).
1283 *What drives metamorphism and metamorphic reactions?* Geological Society,
1284 London Special Publications, **138**, 215–246.
1285 Vitale Brovarone, A., & Agard, P. (2013). True metamorphic isograds or tectonically
1286 sliced metamorphic sequence? New high-spatial resolution petrological data

for the New Caledonia case study. *Contributions to Mineralogy and Petrology*, **166**, 451–469.

Vitale Brovarone, A., Agard, P., Monié, P., Chauvet, A., Rabaute, A. (2018). Tectonic and metamorphic architecture of the HP belt of New Caledonia. *Earth-Science Reviews*, **178**, 48–67.

Vry, J., Powell, R., Golden, K. M., Peterson, K. (2010). The role of exhumation in metamorphic dehydration and fluid production. *Nature Geoscience*, **3**.

Wain, A. L., Waters, D. J. & Austrheim, H. (2001). Metastability of granulites and processes of eclogitisation in the UHP region of western Norway. *Journal of Metamorphic Geology*, **19**, 609–625.

Walsh, E. O. & Hacker, B. R. (2004). The fate of subducted continental margins: two-stage exhumation of the high-pressure to ultrahigh-pressure Western Gneiss Region, Norway. *Journal of Metamorphic Geology*, **22**, 671–687.

Williams, M. L., Scheltema, K. E., Jercinovic, M. J. (2001). High-resolution compositional mapping of matrix phases: implications for mass transfer during crenulation cleavage development in the Moretown Formation, western Massachusetts. *Journal of Structural Geology*, **23**, 923–939.

Wintsch, R., P., Wathen, B. A., McAleer, R. J., Walters, J., Matthews, J. A. (2024). Deformation by pressure solution and grain boundary sliding in a retrograde shear zone in southern New England, USA. *American Journal of Science*, **324**, 17.

Wheeler, J., Piazolo, S., Prior, D. J., Trimby, P. W., & Tielke, J. A. (2024). Using crystal-lattice distortion data for geological investigations: the weighted Burgers vector method. *Journal of Structural Geology*, **179,** 105040.

White, R. W. & Powell, R. (2002). Melt loss and the preservation of granulite facies mineral assemblages. *Journal of Metamorphic Geology*, **20**, 621–632.

White, R. W., Powell, R. & Baldwin, J. (2008). Calculated phase equilibria involving chemical potentials to investigate the textural evolution of metamorphic rocks. *Journal of Metamorphic Geology*, **26,** 181–198.

White, R. W., Powell, R., Holland, T. J. B., Johnson, T. E., Green, E. C. R. (2014a) New mineral activity–composition relations for thermodynamic calculations in metapelitic systems. *Journal of Metamorphic Geology,* **32**, 261–286.

White, R. W., Powell, R. & Johnson, T. E. (2014b). The effect of Mn on mineral stability in metapelites revisited: new *a–x* relations for manganese-bearing minerals. *Journal of Metamorphic Geology*, **32**, 809–828.

Wood, B. J., Holland, T. J. B., Newton, R. C. & Kleppa, O. J. (1980). Thermochemistry of jadeite-diopside pyroxenes. *Geochemica Cosmochimica Acta*, **44**, 1363–1371.

Worley, B., Powell, R., Wilson, C. J. L. (1997). Crenulation cleavage formation: evolving diffusion, deformation and equilibration mechanisms with increasing metamorphic grade. *Journal of Structural Geology*, **19**, 1121–1135.

Yokoyama, K., Brothers, R. N. & Black, P. M. (1986). Regional facies in the high-pressure metamorphic belts of New Caledonia. *Geological Society of America, Memoir*, **164**, 407–423.

Young, D. J. & Kylander-Clark, A. R. C. (2015). Does continental crust transform during eclogite facies metamorphism? *Journal of Metamorphic Geology*, doi: 10.1111/jmg.12123.

ACKNOWLEDGMENTS

Funding was provided by the NERC (NE/X012778/1 to S. P, T. C.), the Faculty of Science at the University of Sydney (G.L.C & T.C), the School of Environmental and Rural Science at the University of New England (T.C). We appreciate the helpful

guidance on the specifics of some THERMOCALC calculations provided by R. Powell. Discussion regarding differing microstructures with R. Vernon also helped frame some of the considerations presented in this work. Helpful and encouraging comments by Simon Schorn and an anonymous reviewer together with the editorial suggestions of Katy Evans help to improve the work.

FIGURE CAPTIONS

Figure 1 (a) geological map of New Caledonia illustrating the major tectonostratigraphic units of the island (modification of Maurizot, 2001). For more details see Chapman & Clarke (2021). (b) regional geological map of NE New Caledonia, indicating the lithological distribution, regional metamorphic zones, and sample localities of the Pam Peninsula and Ouegoá region (after Paris, 1981; Maurizot et al., 1989; Clarke et al., 1997; Fitzherbert et al., 2003). (c) Cross section (labelled on (b)) of the main structural relationships across the Pam Peninsula.

Figure 2 (a) Zone 2b metapelitic schist with pervasive albite porphyroblasts formed during D_3 shearing. The S_3 foliation is defined by chlorite, stilpnomelane, phengite, ferroglaucophane, and quartz. No omphacite is observed. Sample 2021. (b) Banded metasedimentary schist from zone 2a, the lawsonite–epidote transition. S_0 marks composition distinction between glaucophane-rich and omphacite-rich layers. Large, twinned albite porphyroblasts have overgrown glaucophane and omphacite in both layers. The porphyroblasts are larger in the layers without omphacite and are pinned by S_0/S_2. Sample 96321B. (c) Zone 3 metapelitic schist containing weakly aligned omphacite and glaucophane intergrown with garnet and quartz. Sample 9927. (d) large area photomicrograph of zone 3 metapelitic schist with albite poikiloblasts preferentially occurring in strain shadows of garnet or areas of heterogeneous D_3 strain. Sample 9403. (e) Close up from (d) of garnet porphyroblasts wrapped by an S_2

foliation defined by omphacite, glaucophane, phengite, paragonite, and clinozoisite. Coarse S_3 albite poikiloblasts overgrowing S_2 folia comprising omphacite, phengite and garnet. Sample 9403. (f) large area photomicrograph of zone 4 crenulated metapelitic schist. Albite poikiloblasts occur preferentially in dilatational hinge-zones of the S_3 crenulation fabric. Sample 23NC20B. (g) Close-up a crenulation hinge zone with late twinned albite porphyroblasts overgrowing the S_3 crenulation and retaining optical continuity between the twins. Omphacite is present as inclusions in albite poikiloblasts and as grains defining S_3 with phengite, paragonite, graphite, titanite, and garnet. Sample 23NC20B2.

Figure 3 Back-scatter electron images of (a) a zone 1 metapelitic schist comprising lawsonite, phengite, paragonite, albite and glaucophane defining S_2. Sample 2011 (b) high strain metapelitic schist from a D_3 shear zone with remnants of S_2 glaucophane reoriented into S_3. Sample 23NC05A. (c) Large albite with inclusions of jadeite, omphacite and lawsonite from zone 2a. Sample 2013. (d) S_3 crenulation rotating S2 folia comprising omphacite, phengite and paragonite. (e) S_3 albite poikiloblasts have grown in the hinge of S_3 crenulation with inclusions of omphacite, titanite and phengite. The irregular edges involve epitaxial inter-fingering of paragonite (sample 23NC20B2). (f) Omphacite intergrown with phengite and paragonite from Zone 3 metapelitic schist (sample 23NC20B2).

Figure 4 X-ray element maps in weight percent oxide of metapelitic schist sample WC21, (a) Al_2O_3, (b) MgO, (c) Na_2O and (d) CaO. The location of albite porphyroblasts is outlined on maps of Al_2O_3, MgO and CaO to highlight location of omphacite, glaucophane and paragonite crystals and inclusions. (e) Masked Al cation map showing locations of only albite, omphacite, and paragonite. (f) Masked Mg cation map with locations of glaucophane, omphacite, garnet and chlorite.

1390 **Figure 5** EBSD map of albite poikiloblast from sample 2013. (a) a grain reference
1391 orientation deviation (GROD) map of albite together with high-, low-angle and twin
1392 grain boundaries displaying limited crystal distortion. (b) pole figures of jadeite
1393 inclusions within albite displaying coincident crystal axis, locations show by green
1394 and yellow dots in (a). (c) misorientation profile of albite crystal across region
1395 highlight by the arrow in (a).
1396 **Figure 6** EBSD map of albite poikiloblast from sample 9403. (a) a GROD map of
1397 albite displaying limited crystal distortion. Red arrow points to lattice bending in
1398 grain margins pinned against S_3. (b) orientations of unit cell for omphacite inclusion
1399 (green dot) and albite (yellow dot) crystals with coincidence of [010] axes. (c)
1400 misorientation profile of albite crystal across region highlight by the arrow in (a). (d)
1401 pole figures of omphacite inclusions in albite displaying coincident crystal axis.
1402 **Figure 7** EBSD maps of sample 23NC20B2. (a, c) a GROD map of albite, garnet and
1403 omphacite in crenulation domains with high- and low-angle grain boundaries. Red
1404 arrow points to lattice bending in albite grain margins pinned against S_3. (b) GROD
1405 map of quartz across Q- and M-domains, locations of maps (a) and (b) shown by
1406 white rectangles. (d–g) EDS (Na, K, Al) maps of domains of crenulated metapelitic
1407 schist. (h) low-angle boundary misorientation axes pole figures for quartz and
1408 omphacite in crystallographic reference frame.
1409 **Figure 8 (a)** *P–T* pseudosection for Diahot metapelite (WC21) in the
1410 NCKFMASHTO system. Fields of key assemblage zones observed along the Diahot
1411 metamorphic field array are marked (shown by labels Z1, Z2a, Z2b, Z3, Z4) as well
1412 as locations of D_2–D_4 deformation events. Predicted *P–T* paths for different zones
1413 shown, including distinct hairpin (blue) style for zones 1 and 2a relative to zones 2b–4
1414 (grey). (b) pseudosection showing isopleths of H_2O mode (mole %) together with an
1415 inferred *P–T* exhumation path, highlighting locations where the rock passes H_2O-

present (red – +fl [fluid]) and absent conditions (grey – -fl). (c) higher resolution portion of the *P–T* pseudosection focused on the omphacite–albite transition (stippled) bounded by the peristerite gap at higher-*T* and a combination of the lawsonite–epidote transition and two-pyroxene solvus at low-*T*.

Figure 9 (a) $P–M_{H2O}$ pseudosection for Diahot metapelite (WC21) in the NCKFMASHTO system at fixed $T = 460°C$. Proportions of H_2O retained in hydrous minerals from modes in each metamorphic zone are shown by labels (Z1, Z2a, Z2b, Z3, Z4). Decompression paths for fluid-saturated metamorphism are shown in red (*path A*) and involve fluid consumption during albite growth for rocks from zone 2b, and fluid-undersaturated decompression shown in the grey (*path B*) of relevance for zones 3 and 4, a *path C* (in green) requires fluid addition at the omphacite–albite transition to induce transformation. (b) Conjugate $V–M_{H2O}$ pseudosection. The *PT* paths are the same as those in (a) and represent portions of the initially fluid-poor decompression history until intersection of the omphacite–albite transition marked by the stippled field.

Figure 10 (a) *V–T* pseudosection for Diahot metapelite (WC21) in the NCKFMASHTO system over the same *T* conditions as Figure 8a. Isobars are shown in black and conditions of Diahot metamorphic zonesare labelled. Many narrow low-variance field in the *P–T* pseudosection are enlarged in the conjugate *V–T* pseudosection, the studied omphacite–albite transition is marked by the stippled field. (b) pseudosection showing isopleths of H_2O mode (mole %) together with an inferred *P–T* exhumation path, inclusive of locations where the rock passes H_2O-present (red – +fl) and absent conditions (grey [*path B*]– -fl). Additional metastable *path A* in green is discussed in the text. (c) expanded portion of the *V–T* pseudosection focused on the omphacite–albite transition (stippled) bounded by the peristerite gap at higher-*T*.

Figure 11 proportion of H_2O (mole %) (a) and density (ρ) (b) predicted versus observed in mineral assemblages for metapelite in each zone and a D_3 shear zone. Volume change (ΔV) (c) related to extent of retrogression (ξ) (d) from peak metamorphic conditions, versus predicted change assuming fully re-equilibration. (e–f) observed versus predicted modal ratios of paragonite (light purple), albite (light blue), and sodic–calcic clinopyroxene (green).

Figure 12 Structural progression for Diahot terrane metapelitic schists showing schematics of zones of albite–omphacite–paragonite intergrowths in domains of dilation from S_3 crenulation cleavage or D_3 shear zones.

Supplement

Figure S1 (a) EBSD GROD map of high strain sample 23NC05A showing distortion in albite, glaucophane and quartz with overlaid high- and low-angle boundary distribution. The S_2 foliation is preserved as inclusion trails in glaucophane at an oblique angle to S_3. (b & c) Al and Na EDS maps over the same area as (a).

Figure S2 Pole figures from high strain sample 23NC05A for quartz (a), glaucophane (b), clinozoisite (c), chlorite (d) and albite (f).

Figure S3 Pole figures from crenulated sample 23NC20B2 for quartz (a), clinozoisite (b), omphacite (c), paragonite (d), and titanite (e).

Table S1 representative bulk–rock compositions.

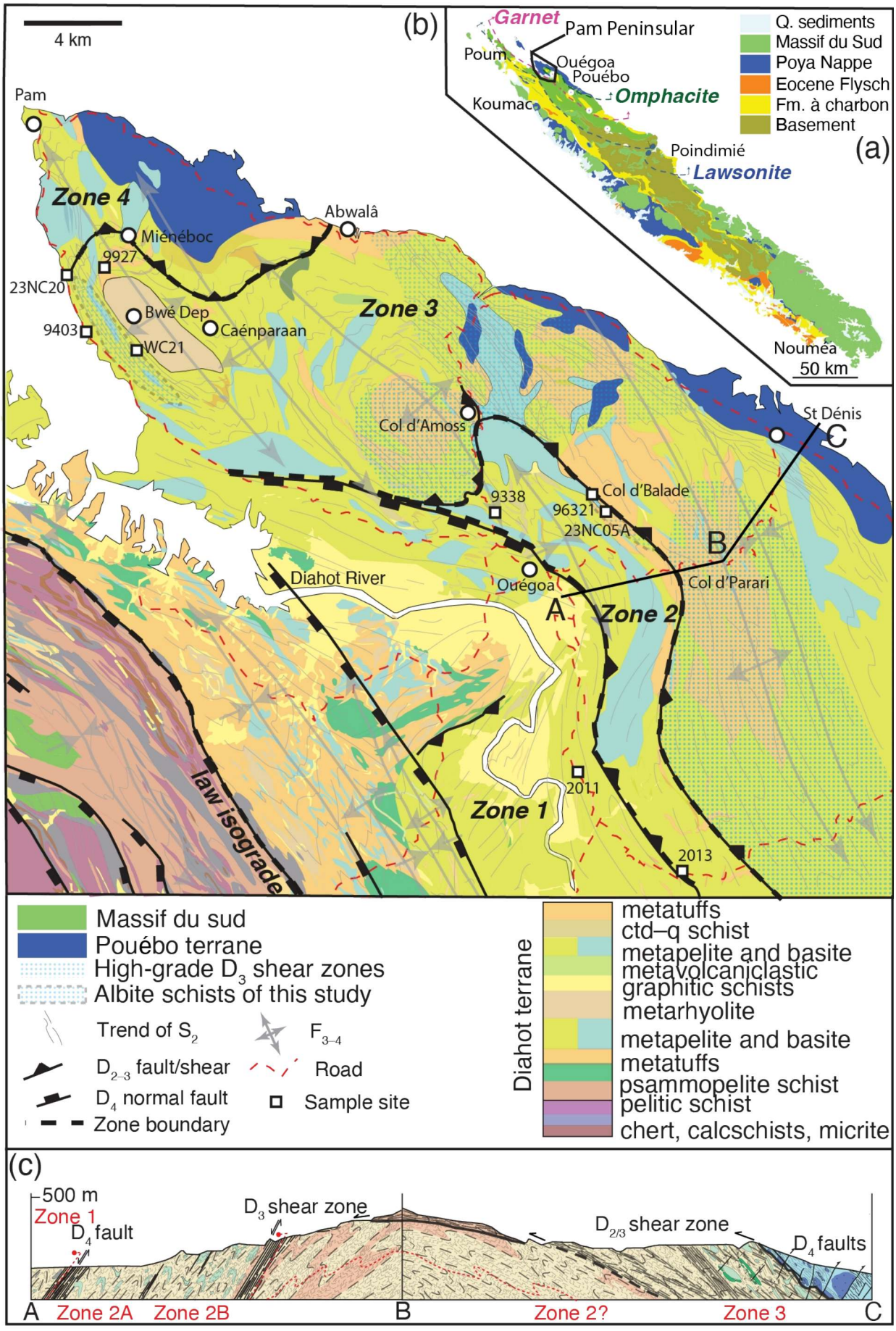
(b)
4 km
Pam
Zone 4
Mienéboc
9927
23NC20
Bwé Dep
Caénparaan
9403
WC21
Abwalâ
Zone 3
Col d'Amoss
9338
Col d'Balade
96321
23NC05A
St Dénis
C
B
Diahot River
Ouégoa
A
Col d'Parari
Zone 2
2011
Zone 1
2013
law isograde
(a)
Garnet
Pam Peninsular
Poum
Ouégoa
Pouébo
Omphacite
Koumac
Poindimié
Lawsonite
Nouméa
50 km
Q. sediments
Massif du Sud
Poya Nappe
Eocene Flysch
Fm. à charbon
Basement
Massif du sud
Pouébo terrane
High-grade D3 shear zones
Albite schists of this study
Trend of S2
F3–4
D2–3 fault/shear
Road
D4 normal fault
Sample site
Zone boundary
Diahot terrane
metatuffs
ctd–q schist
metapelite and basite
metavolcaniclastic
graphitic schists
metarhyolite
metapelite and basite
metatuffs
psammopelite schist
pelitic schist
chert, calcschists, micrite
(c)
500 m
Zone 1
D4 fault
D3 shear zone
D2/3 shear zone
D4 faults
A
Zone 2A
Zone 2B
B
Zone 2?
Zone 3
C

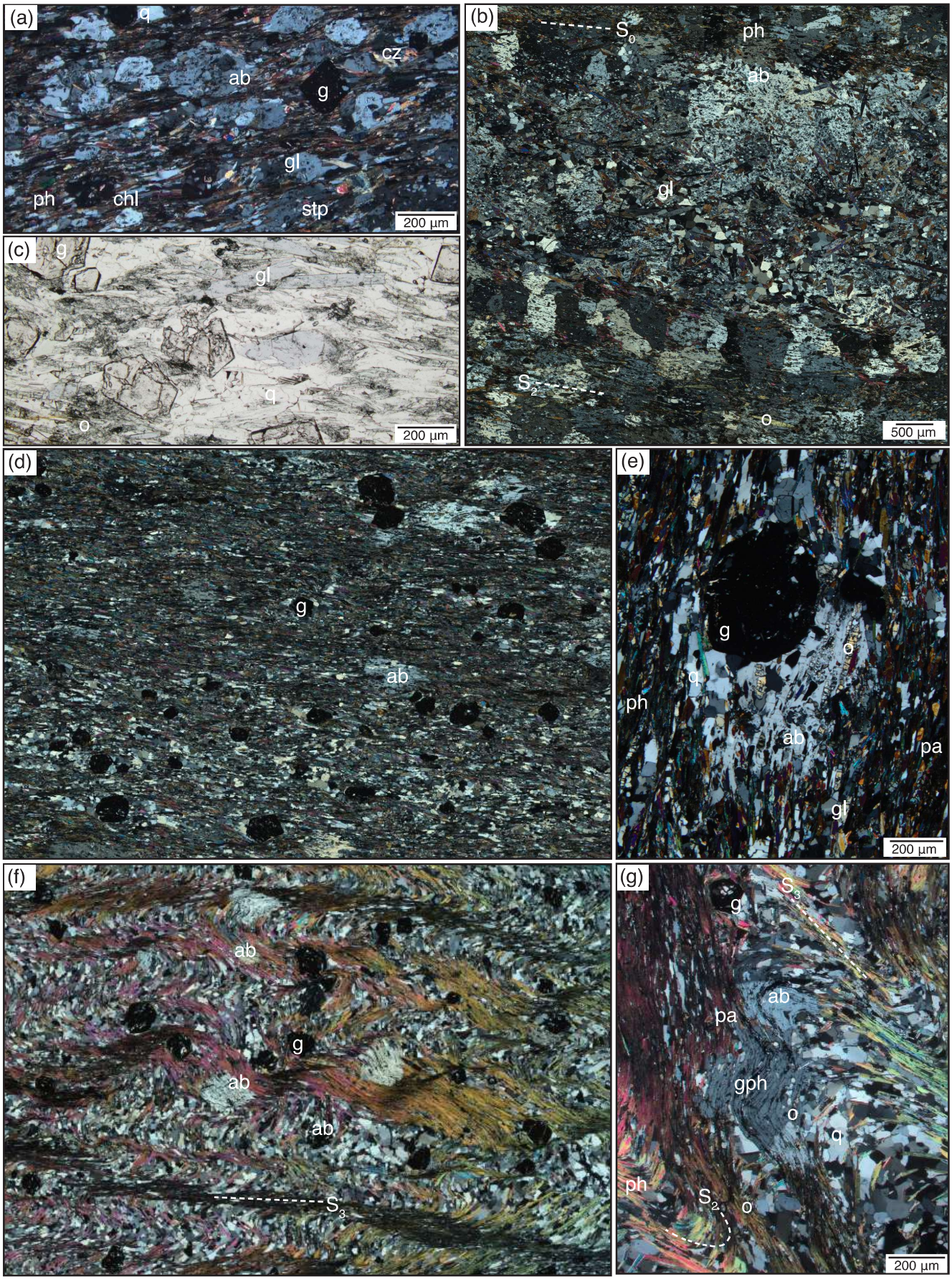

Chapman et al. Figure 2

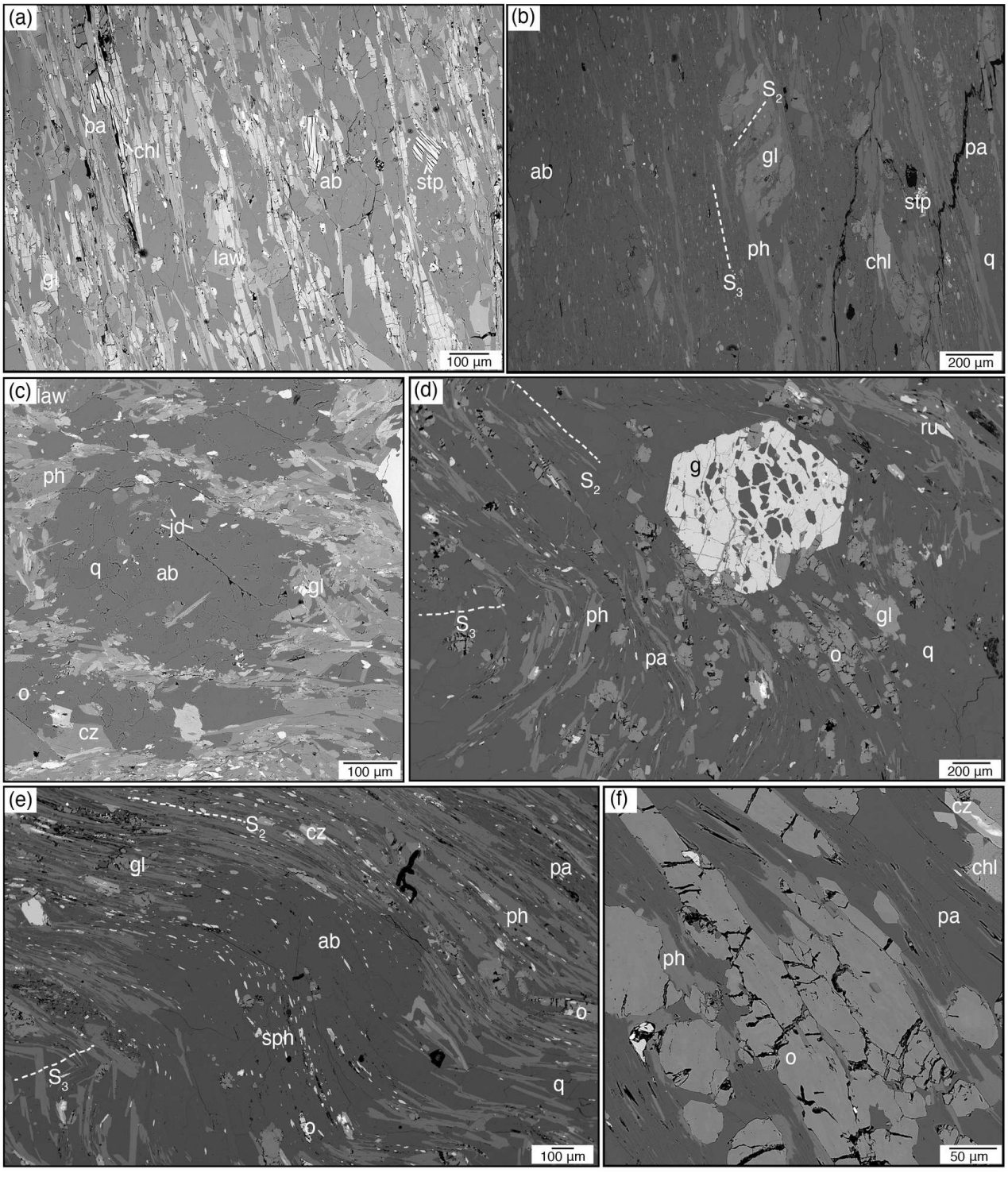

Chapman et al. Figure 3

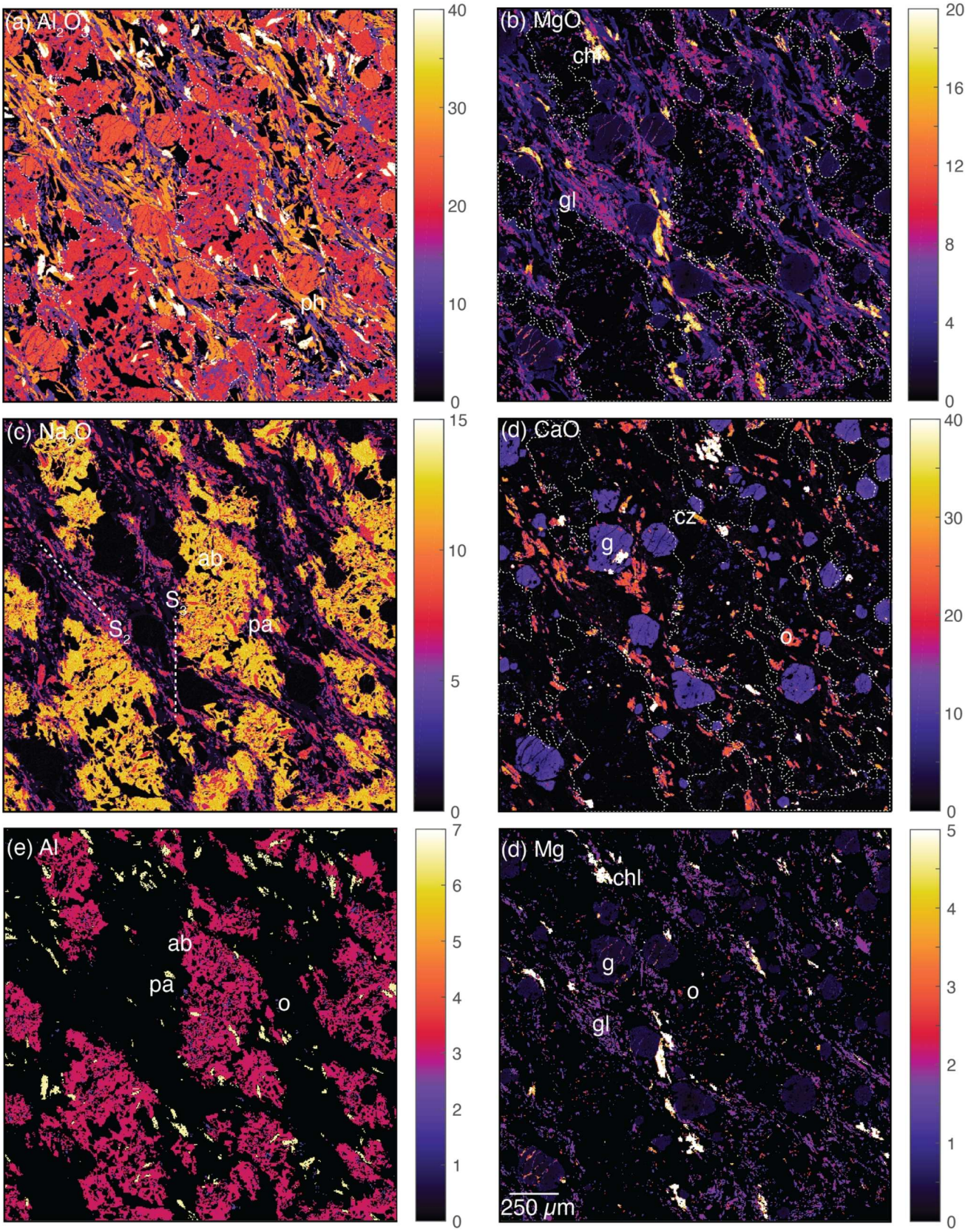

Chapman et al. Figure 4

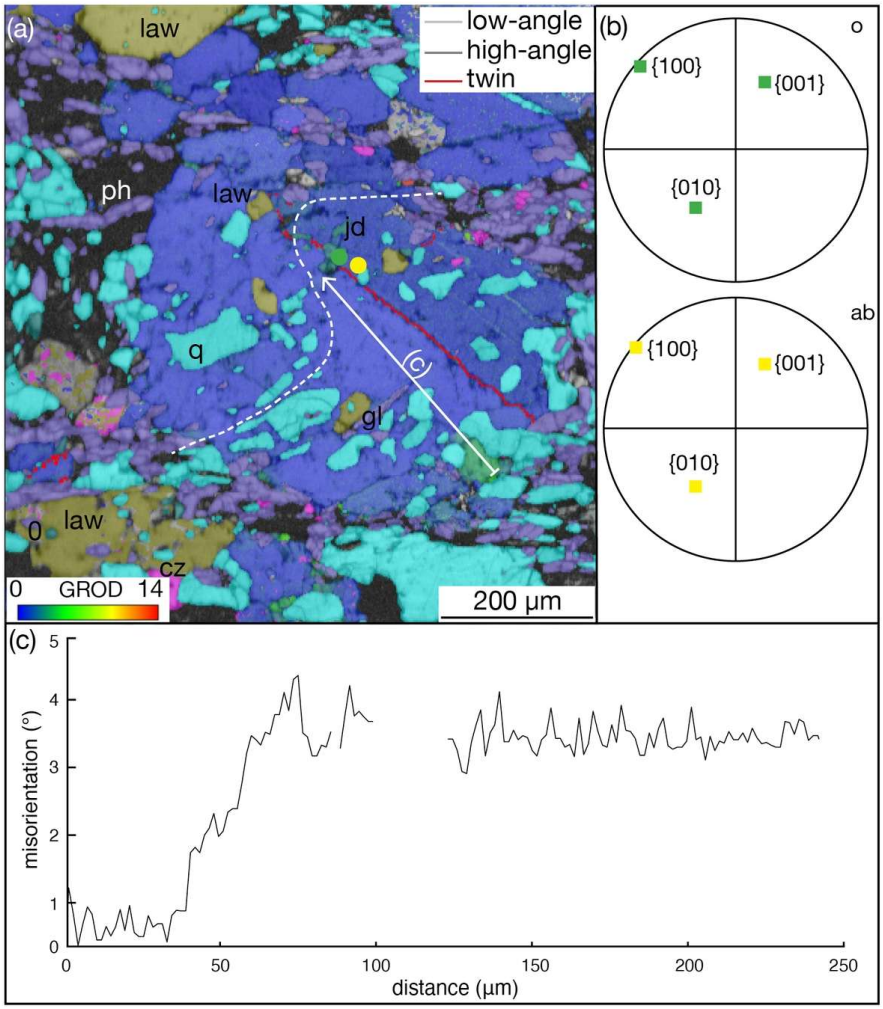
(a)
law
low-angle
high-angle
twin
ph
law
jd
q
(c)
gl
law
0
cz
0 GROD 14
200 µm
(b)
o
{100}
{001}
{010}
ab
{100}
{001}
{010}
(c)
misorientation (°)
distance (µm)
0
1
2
3
4
5
0
50
100
150
200
250

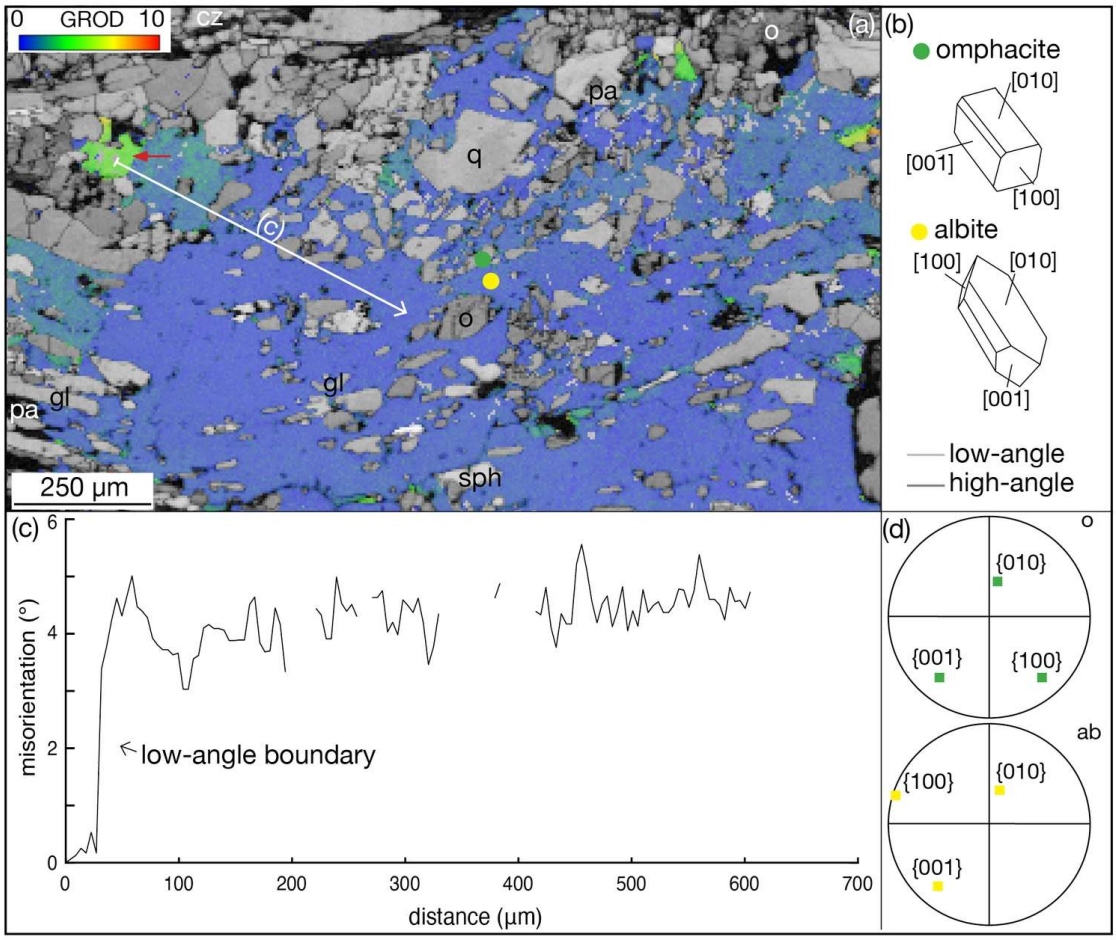

Chapman et al. Figure 6

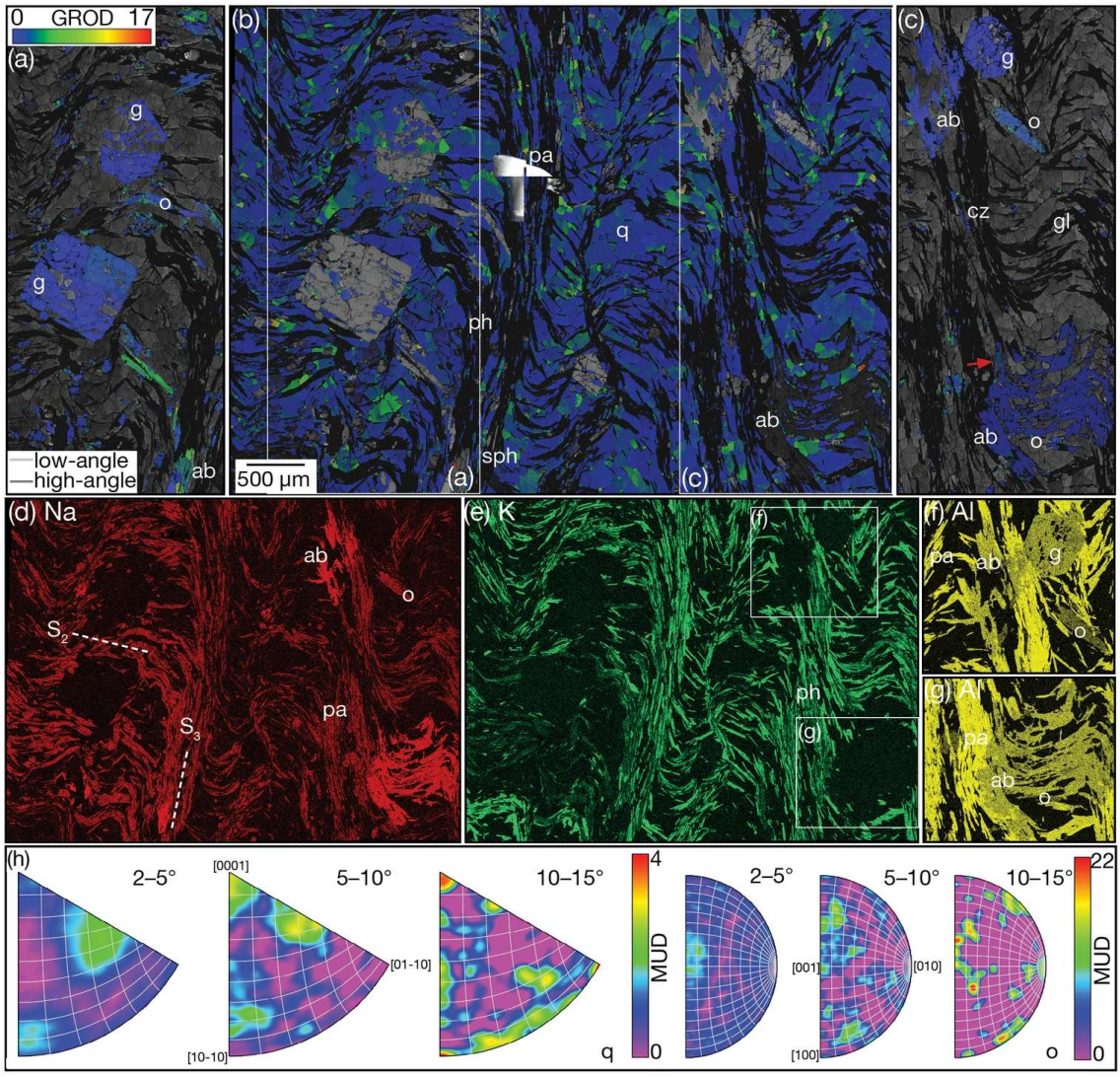

Chapman et al. Figure 7

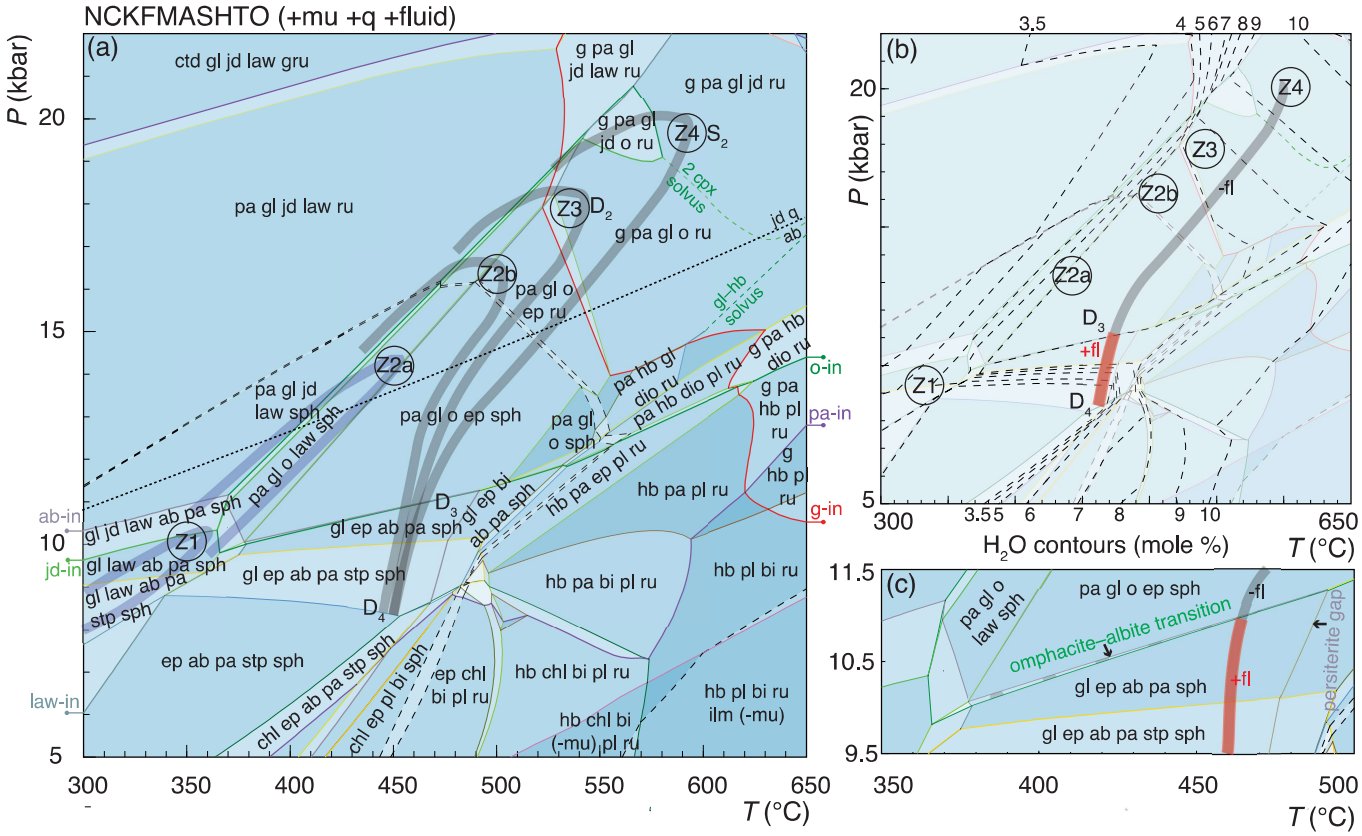
NCKFMASHTO (+mu +q +fluid)
(a)
(b)
(c)
P (kbar)
T (°C)
H2O contours (mole %)
ctd gl jd law gru
g pa gl jd law ru
g pa gl jd ru
g pa gl jd o ru
pa gl jd law ru
g pa gl o ru
pa gl o ep ru
pa gl jd law sph
pa gl o ep sph
pa gl o sph
pa hb gl dio ru
pa hb dio pl ru
g pa hb dio ru
g pa hb pl ru
g hb pl ru
hb pa pl ru
gl jd law ab pa sph
gl ep ab pa sph
gl law ab pa sph
gl ep ab pa stp sph
stp sph
ep ab pa stp sph
chl ep ab pa stp sph
chl ep pl bi sph
ep chl bi pl ru
hb pa bi pl ru
hb pl bi ru
hb chl bi pl ru
hb chl bi (-mu) pl ru
hb pl bi ru ilm (-mu)
Z1
Z2a
Z2b
Z3
Z4
D2
D3
D4
S2
2 cpx solvus
jd q ab
gl–hb solvus
ab-in
jd-in
law-in
o-in
pa-in
g-in
+fl
-fl
omphacite–albite transition
persiterite gap

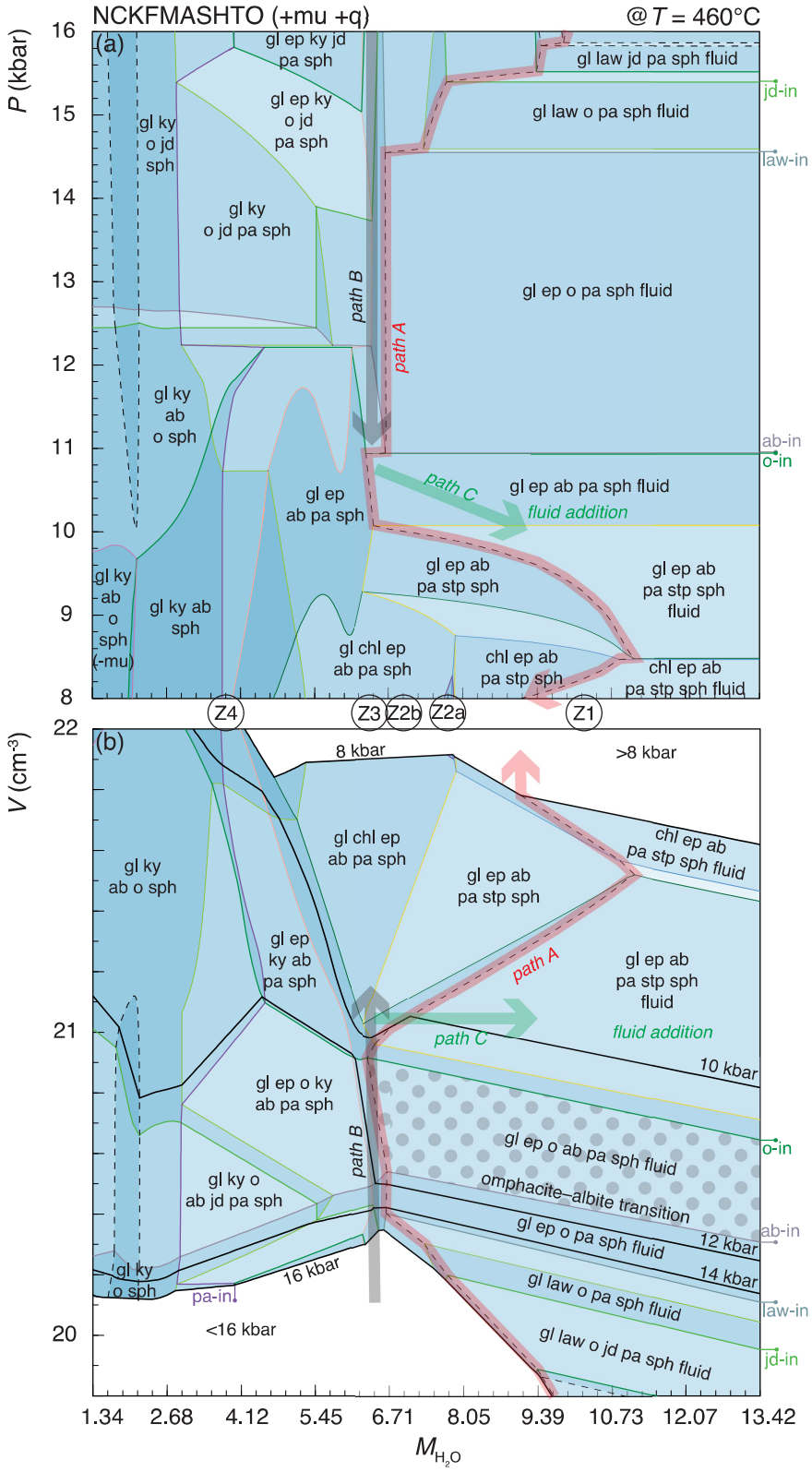
NCKFMASHTO (+mu +q)
@ T = 460°C
(a)
P (kbar)
16
15
14
13
12
11
10
9
8
gl ep ky jd pa sph
gl ky o jd sph
gl ep ky o jd pa sph
gl ky o jd pa sph
gl law jd pa sph fluid
jd-in
gl law o pa sph fluid
law-in
path B
path A
gl ep o pa sph fluid
gl ky ab o sph
ab-in
o-in
path C
gl ep ab pa sph
gl ep ab pa sph fluid
fluid addition
gl ep ab pa stp sph
gl ep ab pa stp sph fluid
gl ky ab o sph (-mu)
gl ky ab sph
gl chl ep ab pa sph
chl ep ab pa stp sph
chl ep ab pa stp sph fluid
Z4
Z3
Z2b
Z2a
Z1
(b)
V (cm-3)
22
21
20
8 kbar
>8 kbar
gl ky ab o sph
gl chl ep ab pa sph
chl ep ab pa stp sph fluid
gl ep ab pa stp sph
gl ep ky ab pa sph
path A
gl ep ab pa stp sph fluid
path C
fluid addition
10 kbar
gl ep o ky ab pa sph
path B
o-in
gl ep o ab pa sph fluid
omphacite–albite transition
gl ky o ab jd pa sph
ab-in
12 kbar
gl ep o pa sph fluid
14 kbar
gl ky o sph
pa-in
16 kbar
gl law o pa sph fluid
law-in
<16 kbar
gl law o jd pa sph fluid
jd-in
1.34
2.68
4.12
5.45
6.71
8.05
9.39
10.73
12.07
13.42
M H2O

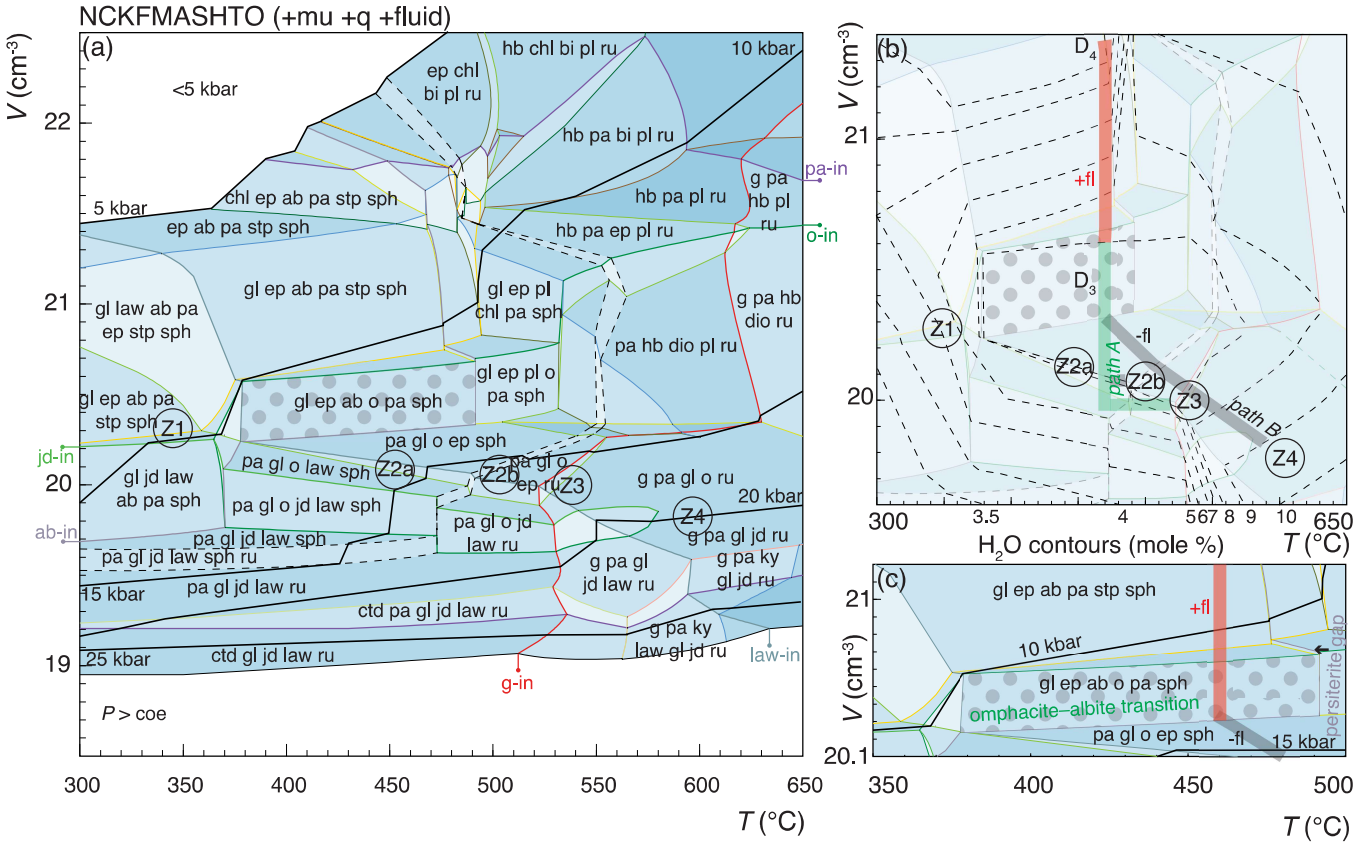
NCKFMASHTO (+mu +q +fluid)
(a)
<5 kbar
5 kbar
15 kbar
20 kbar
25 kbar
10 kbar
ep chl bi pl ru
hb chl bi pl ru
hb pa bi pl ru
chl ep ab pa stp sph
ep ab pa stp sph
hb pa pl ru
hb pa ep pl ru
g pa hb pl ru
gl ep ab pa stp sph
gl ep pl chl pa sph
gl law ab pa ep stp sph
g pa hb dio ru
pa hb dio pl ru
gl ep ab pa stp sph
gl ep ab o pa sph
gl ep pl o pa sph
pa gl o ep sph
pa gl o law sph
pa gl o ep ru
gl jd law ab pa sph
pa gl o jd law sph
g pa gl o ru
pa gl o jd law ru
g pa gl jd ru
pa gl jd law sph
pa gl jd law sph ru
g pa gl jd law ru
g pa ky gl jd ru
pa gl jd law ru
ctd pa gl jd law ru
g pa ky law gl jd ru
ctd gl jd law ru
Z1
Z2a
Z2b
Z3
Z4
pa-in
o-in
jd-in
ab-in
g-in
law-in
P > coe
V (cm-3)
T (°C)
(b)
D4
D3
+fl
-fl
path A
path B
H2O contours (mole %)
(c)
gl ep ab pa stp sph
10 kbar
gl ep ab o pa sph
omphacite–albite transition
pa gl o ep sph
15 kbar
coesite/quartz gap

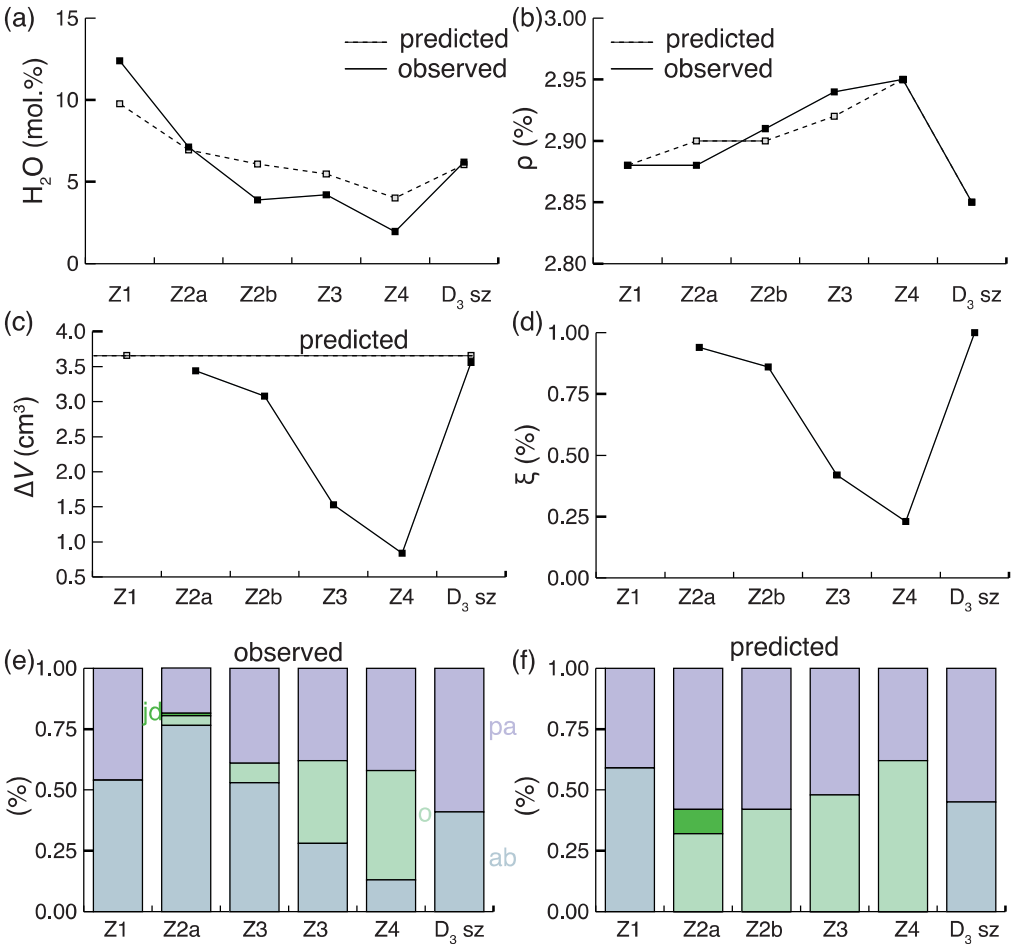
(a)
predicted
observed
H2O (mol.%)
15
10
5
0
Z1
Z2a
Z2b
Z3
Z4
D3 sz
(b)
predicted
observed
ρ (%)
3.00
2.95
2.90
2.85
2.80
(c)
predicted
ΔV (cm3)
4.0
3.5
3.0
2.5
2.0
1.5
1.0
0.5
(d)
ξ (%)
1.00
0.75
0.50
0.25
0.00
(e)
observed
(%)
jd
pa
c
ab
(f)
predicted

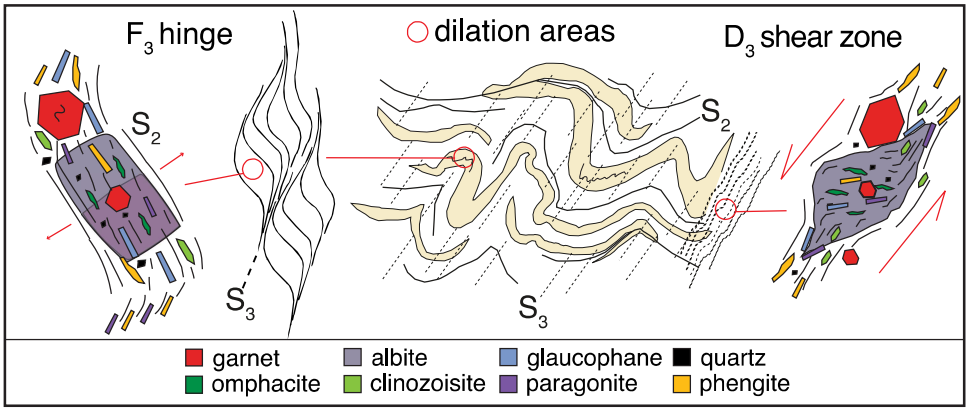
F3 hinge
dilation areas
D3 shear zone
S2
S3
S2
S3
garnet
omphacite
albite
clinozoisite
glaucophane
paragonite
quartz
phengite

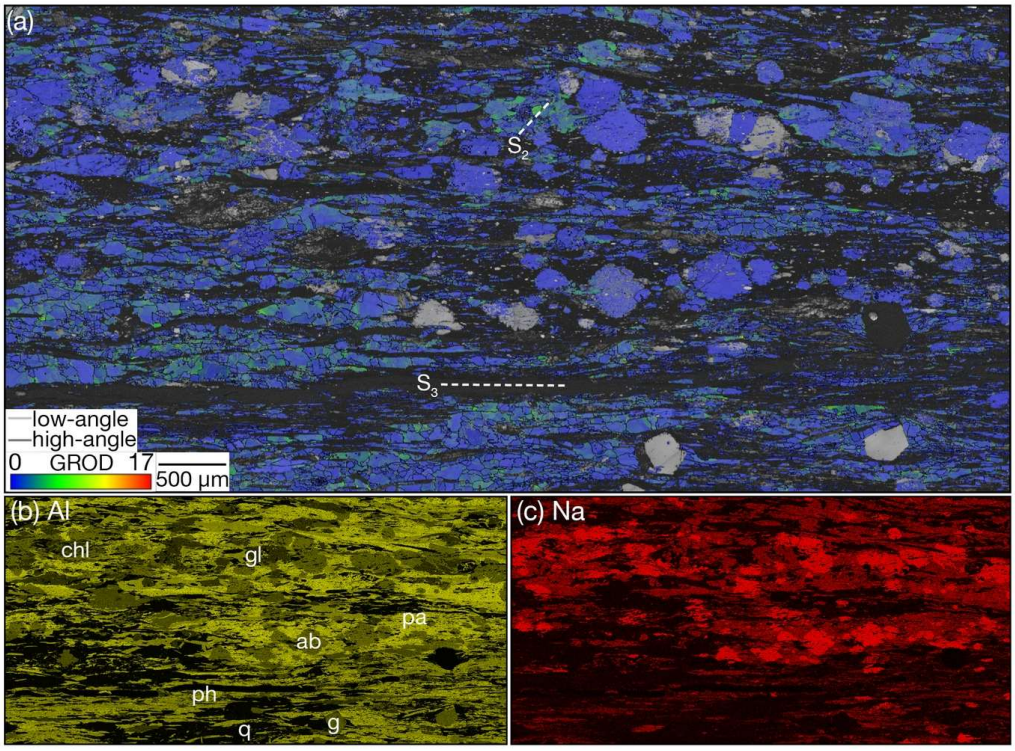

Chapman et al. Figure S1

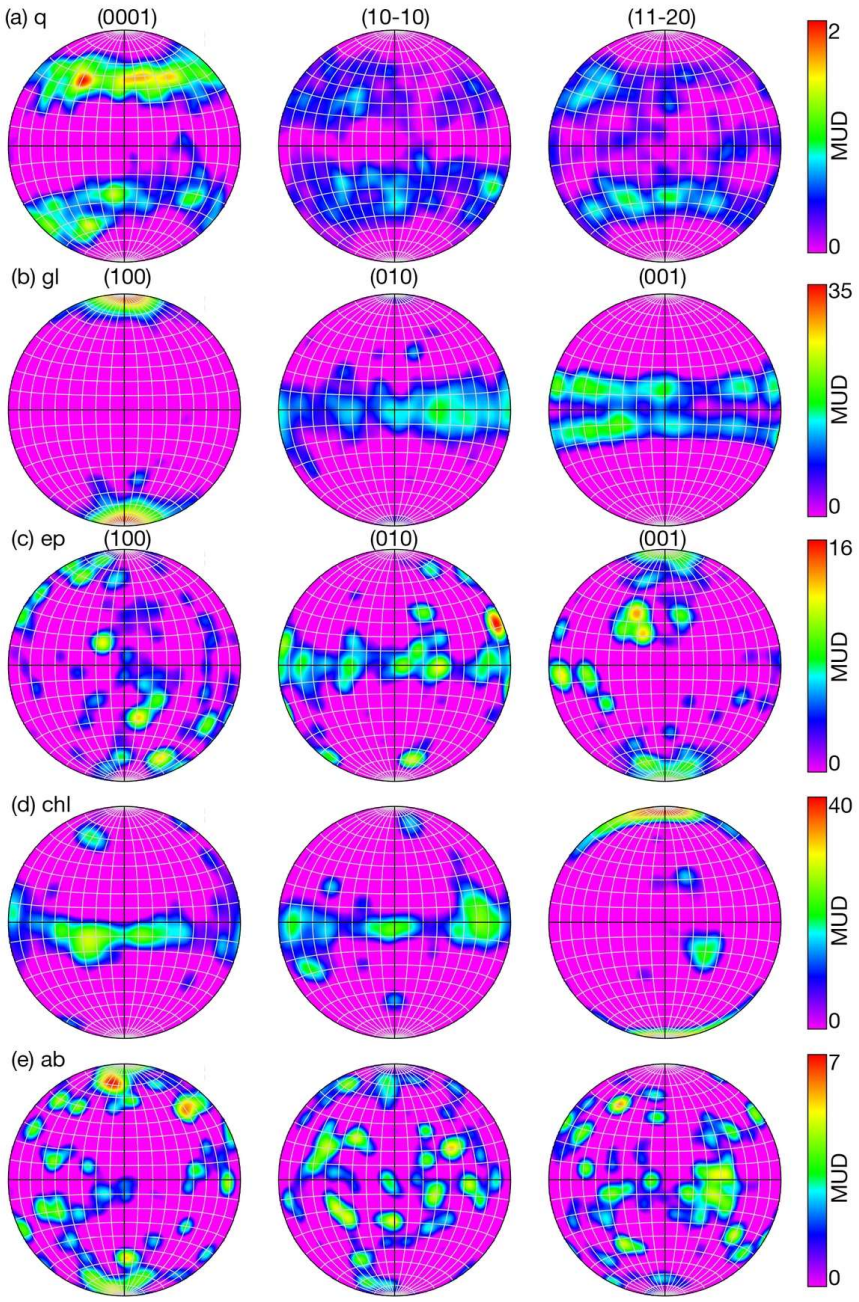

Chapman et al. Figure S2

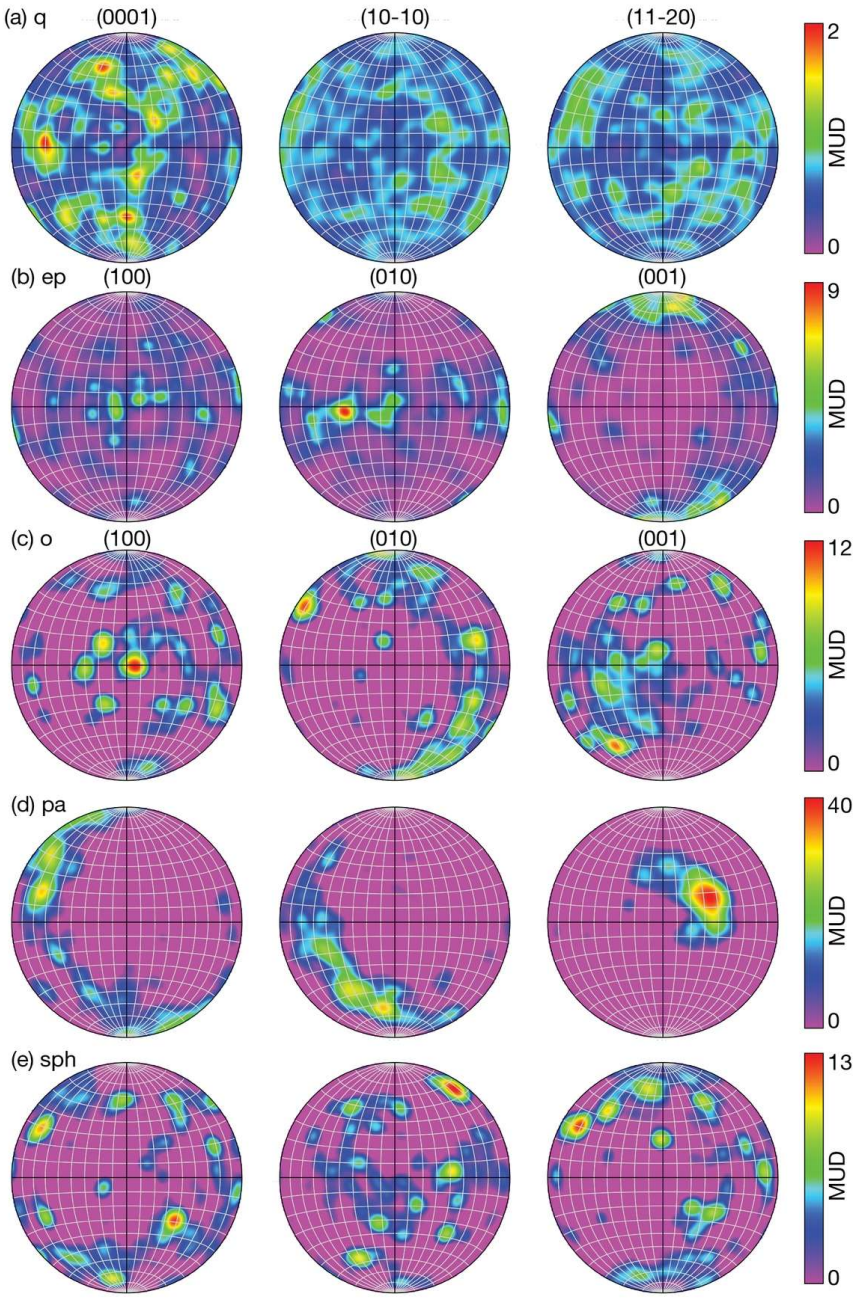

Chapman et al. Figure S3

Table S1 weight percent oxide of metapelite bulk composition from the Diahot Terrane and Diahot metaseidment average

isozone	sample	SiO_2	TiO_2	Al_2O_3	FeO	MnO	MgO	CaO	Na_2O	K_2O	O	H_2O
Z2a	2013	67.35	0.93	15.89	3.97	0.14	1.94	3.02	4.50	2.40	-	-
Z2b	23NC05A	68.90	0.62	16.25	5.08	0.13	1.44	2.10	1.96	2.41	-	-
Z3	9403	65.10	0.80	17.12	4.44	0.05	2.18	2.19	1.87	5.43	-	-
Z3	WC21	64.89	0.80	16.28	6.09	0.49	2.15	3.09	4.85	0.86	-	-
Z4	9927	67.46	0.85	15.02	4.66	0.24	1.81	3.76	4.37	1.47	-	-
Z4	23NC20B2	67.22	0.45	16.68	6.16	0.08	2.28	2.21	1.79	3.15	-	-
n = 138	average	65.96	0.84	15.87	5.97	0.34	3.18	2.99	2.58	1.93	-	-
modelled	WC21	60.51	0.57	9.09	4.83	0.00	3.04	3.14	4.45	0.52	0.44	13.42